Computer Modeling in Engineering & Sciences

Tech Science Press

https://doi.org/10.32604/cmes.2026.079067

ARTICLE

Optimal Resource Allocation in a Bacterial Growth Model Under Cold Stress and Temperature

Saira Batool*, Muhammad Imran* and Brett McKinney*

Tandy School of Computer Science, University of Tulsa, Tulsa, OK, USA

*Corresponding Authors: Saira Batool. Email: saira-batool@utulsa.edu; Muhammad Imran. Email: muhammad-imran@utulsa.edu; Brett McKinney. Email: brett-mckinney@utulsa.edu

Received: 14 January 2026; Accepted: 03 March 2026; Published: 30 March 2026

ABSTRACT: Bacterial growth requires strategic allocation of limited intracellular resources, especially under cold stress, where stabilized messenger ribonucleic acid (mRNA) secondary structures slow translation by impairing ribosome binding. *Escherichia coli* (*E. coli*) counters this bottleneck by inducing the cold-shock protein A (CspA), an RNA chaperone that remodels inhibitory structures. However, synthesizing CspA diverts biosynthetic capacity from ribosome production and metabolism, creating a fundamental resource-allocation trade-off. In this work, we develop a dynamical model capturing the interplay between metabolic precursors, ribosomes, and CspA, and use it to examine how growth and allocation patterns shift with temperature. Steady-state analysis shows that each temperature produces a distinct, locally stable equilibrium, illustrating how cold environments reshape cellular priorities. We then formulate growth maximization as an optimal control problem, solved using Pontryagin's Maximum Principle, to identify allocation strategies that balance translation maintenance and biomass production. The resulting optimal strategies exhibit bang-bang and singular structures, highlighting periods of extreme and intermediate allocation that reflect how bacteria might dynamically prioritize competing cellular functions. These control patterns converge to their corresponding steady state allocations and provide quantitative insight into optimal resource management under cold stress. These results provide a quantitative optimal-control framework linking RNA-level cold-shock adaptation to proteome allocation and growth, yielding testable predictions for how bacteria balance translational maintenance and biomass production at suboptimal temperatures.

KEYWORDS: Bacterial growth; resource allocation; nonlinear dynamical systems; singular regime; optimal control analysis

1 Introduction

Microorganisms are constantly exposed to fluctuations in their environment, particularly in nutrient availability and temperature. To survive and thrive under such conditions, they have evolved sophisticated strategies that enable dynamic physiological adaptation [1]. This adaptation is primarily achieved through large-scale reorganization of gene expression, including regulation of genes responsible for nutrient uptake, energy production, protein synthesis, and stress responses [2,3]. Central to this process is the efficient allocation of cellular resources, particularly protein synthesis capacity, across competing functional demands [4–6]. Among environmental variables, temperature is especially influential, directly affecting reaction kinetics, enzyme activity, and the stability of cellular structures [7]. Under cold stress, biochemical reactions slow markedly, and energy availability becomes limited, intensifying the challenge of maintaining balanced resource allocation [1].

Exposure to low temperatures triggers extensive physiological reorganization, including the redistribution of limited resources such as ribosomes, metabolic enzymes, and energy toward essential survival functions. In these conditions, messenger RNA (mRNA) molecules tend to form stable secondary structures, such as hairpins, that impede ribosome binding and slow translation, thereby reducing protein synthesis efficiency [1]. To overcome these obstacles, *Escherichia coli* induces cold-adaptive proteins (CSPs), particularly CspA, which is rapidly upregulated under low temperatures and can constitute up to 10% of total cellular protein, reaching intracellular concentrations around 100 μM [8–10]. Acting as RNA chaperones, CSPs destabilize inhibitory secondary structures in nucleic acids, facilitating efficient transcription and translation during cold adaptation and thereby restoring cellular homeostasis under low-temperature conditions.

CspA functions primarily as an RNA chaperone, binding transiently to single-stranded regions of mRNA with low sequence specificity and moderate affinity [8,11]. It binds cooperatively to single-stranded RNA stretches longer than 74 nucleotides, with a minimal concentration of approximately 2.7×10^{-5} M required for cooperative binding, well below the levels observed in cells under cold conditions (1×10^{-4} M) [8]. Functionally, CspA destabilizes inhibitory secondary structures of RNA, preventing the formation of stable hairpins that impede translation and making mRNA more accessible to ribosomes and ribonucleases. Multiple CspA molecules can bind concurrently to a single mRNA transcript, remodeling stabilized secondary structures at low temperatures and facilitating efficient translation initiation. By improving ribosome accessibility and translational efficiency, CspA plays a central role in maintaining protein synthesis capacity when low temperatures slow cellular processes [12].

Experimental studies indicate that low temperatures reduce translation efficiency due to stabilization of mRNA secondary structures, limiting protein synthesis and growth. To cope with this challenge, *E. coli* induces cold-shock protein CspA, which alleviates inhibitory RNA structures [9,12]. However, the synthesis of CspA consumes significant cellular resources, creating a trade-off. Excessive CspA production competes with ribosome biogenesis and other essential processes, potentially limiting overall growth. This suggests the existence of an optimal CspA level that balances the benefits of enhanced translation against the costs of resource allocation, providing a natural framework for applying optimal control theory to quantify growth strategies under cold-shock conditions. Optimal control provides a theoretical benchmark for quantifying such growth strategies under cold-shock conditions [13,14], and although exact optimal strategies are unlikely to be implemented physiologically, they represent a gold standard that can be used to evaluate how closely real bacterial regulatory mechanisms approximate optimal resource allocation.

Microbial growth and resource allocation have been extensively investigated from both experimental and theoretical perspectives [7,13,14]. Early systems-biology studies established empirical growth laws linking ribosome content, proteome partitioning, and cellular growth rate, revealing fundamental trade-offs in bacterial resource economics [15–17]. Building on these biological insights, several theoretical frameworks have sought to formalize microbial growth optimization using mathematical and control-theoretic approaches. For instance, Giuliodori et al. [12] formulated microbial growth in fluctuating environments as an optimal control problem, while Yegorov et al. [13,14] extended this work to include protein degradation, recycling, and temperature-dependent kinetics. More recently, Mairet et al. examined proteome allocation under temperature stress, showing that extreme conditions redirect resources to chaperone-mediated repair processes [18]. Despite these advances, quantitative models that specifically capture low-temperature adaptation and its associated trade-offs in *Escherichia coli* remain limited. Addressing this gap, the present study develops a dynamical model to investigate how bacteria allocate limited translational resources to balance growth and stress adaptation under cold-shock conditions.

Building on these principles, we formulate a dynamical model of *E. coli* under low temperature using ordinary differential equations (ODEs) to describe the interplay between ribosomes, metabolism, and CspA.

The RNA-chaperone activity of CspA is represented by a modulation factor applied to the effective protein-synthesis rate, reflecting its role in alleviating inhibitory mRNA secondary structures. To focus on the primary trade-off between translation efficiency and ribosomal availability, we assume that other regulatory factors and stress responses not directly related to ribosome or CspA allocation are negligible. For the purpose of this model, we assume that CspA-mediated translation is the main mechanism driving adaptation under low temperatures. Under these assumptions, ribosome and CspA synthesis are dynamically regulated to maximize cumulative growth, defined as the total increase in cellular components (ribosomes, CspA, and metabolic intermediates), over a defined time horizon. Resource allocation is formulated as a dynamic optimal control problem in which the objective is to maximize cumulative cellular growth over a defined time horizon. In this framework, the control variables represent the fractional distribution of translational resources between ribosome synthesis and CspA production. Applying Pontryagin's Maximum Principle yields the necessary conditions for optimal resource allocation and enables the identification of candidate strategies that balance growth with stress adaptation. This formulation supports the analysis of both open-loop and feedback control policies, offering insights into how temporal dynamics and environmental conditions shape optimal bacterial growth trajectories under cold-shock stress.

Overall, this study introduces a quantitative framework that integrates molecular cold-shock mechanisms with optimal resource allocation principles. By explicitly linking RNA-level adaptation to proteome allocation and growth optimization, the model offers new insight into how *E. coli* balances translational efficiency and biomass production at suboptimal temperatures. The results generate testable predictions for cold-shock adaptation and provide a foundation for future experimental and theoretical investigations into microbial growth strategies under low-temperature stress. The paper is organized as follows. Section 2 outlines the mathematical framework governing the dynamical model. Section 3 analyzes temperature-dependent steady states and stability. Section 4 introduces the optimal control problem and characterizes optimal allocation strategies. Section 5 presents the key conclusions and highlights potential directions for future research.

2 Formulation

Consider a population of self-replicating prokaryotic cells, such as *Escherichia coli*, in a continuous stirred-tank reactor (CSTR) of constant volume. Let P, M, R, and C [g] denote the total masses of precursor metabolites (amino acids), metabolic machinery (enzymes involved in the uptake and conversion of nutrients into precursors), gene expression machinery (polymerases and ribosomes), and the cold-shock protein CspA, respectively. The metabolic machinery converts external substrates into precursors, while the gene-expression machinery and CspA utilize these precursors to synthesize the macromolecules required for cellular growth and maintenance. A schematic diagram (Fig. 1) illustrates the mass fluxes and catalytic interactions within the system. Based on the mass balances of these components, the system dynamics are described by a controlled set of ordinary differential equations (ODEs) that capture the time evolution of precursors, metabolic enzymes, ribosomes, and CspA (Eq. (1)). Unlike classical microbial growth models in which translational efficiency is prescribed as a fixed or externally scaled parameter, the present formulation treats translation as an endogenous, state-dependent process modulated by the intracellular concentration of the cold-shock protein CspA.

$$\frac{dP}{dt} = V_M - f(C)V_R,$$
$$\frac{dM}{dt} = (1-\alpha)(1-\beta)f(C)V_R - \gamma_M M(t),$$

$$\frac{dR}{dt} = \alpha(1-\beta)f(C)V_R - \gamma_R R(t),$$
$$\frac{dC}{dt} = \beta f(C)V_R - \gamma_C C(t), \tag{1}$$

with following initial conditions,

$$P(0) = P_0 \geq 0,\ M(0) = M_0 \geq 0,$$
$$R(0) = R_0 \geq 0,\ C(0) = C_0 \geq 0,$$

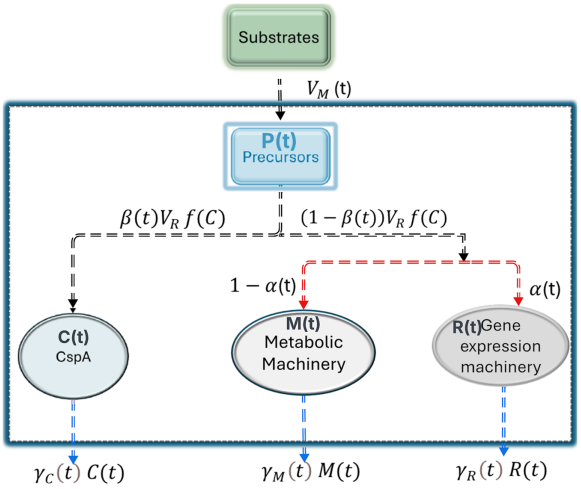

Figure 1: Flow diagram represents the flow or distribution of nutrients between different parts of the cellular machinery.

where $f(C)$ denotes the CspA-dependent modulation of translational efficiency, V_M and V_R are the metabolic and translational fluxes, respectively, $t \in [0, T]$ (hours) is the time variable, and T is the time horizon. A detailed description of each parameter and function involved in the proposed model (Eq. (1)) can be found as follows:

- $V_M = V_M(t)$ $[\mathrm{g} \cdot h^{-1}]$ is the metabolic flux, i.e., the rate at which precursor metabolites P are synthesized by the metabolic machinery M from external nutrients.
- $V_R = V_R(t)$ $[\mathrm{g} \cdot \mathrm{h}^{-1}]$, modulated by $f(C)$, denotes the effective translational flux, i.e., the rate at which ribosomes R consume precursor metabolites to synthesize cellular proteins. In contrast to classical growth models where translational efficiency is prescribed as a fixed or externally scaled parameter, V_R here is an endogenous, state-dependent quantity regulated by the intracellular concentration of the cold-shock protein CspA. The modulation function $f(C)$ accounts for the RNA-chaperone activity of CspA under cold-shock conditions, whereby destabilization of inhibitory mRNA secondary structures enhances ribosome accessibility and protein synthesis efficiency.
- $\gamma_M > 0$ $[\mathrm{h}^{-1}]$, $\gamma_R > 0$ $[\mathrm{h}^{-1}]$ and $\gamma_C > 0$ $[\mathrm{h}^{-1}]$ represent the degradation rates of the metabolic machinery M, gene expression machinery R and cold shock protein C, respectively.
- $\beta = \beta(t)$ and $\alpha = \alpha(t)$ are dimensionless resource allocation functions (control strategies), such that at any time $t \in [0, T]$, $\beta(t)$ represents the fraction of precursor mass allocated to CspA, while the remaining fraction $1-\beta(t)$ is divided between ribosomes and metabolic machinery according to $\alpha(t)$ and $1-\alpha(t)$, respectively.
- $\alpha \in [0, 1]$ and $\beta \in [0, 0.2]$ denote the admissible range of resource allocation fractions.

- Cells in the population are assumed to share a constant cytoplasmic density, with $\delta > 0$ $[\mathrm{L}\cdot\mathrm{g}^{-1}]$ representing its inverse.
- The structural volume of the cell population is defined as

$$V(t) = \beta \cdot (M(t) + R(t) + C(t)) \quad [\mathrm{L}] \tag{2}$$

representing the volume occupied by the macromolecules of the metabolic and gene expression machinery and cspA, excluding monomeric precursors.

- The concentrations of the cellular components are defined as

$$p(t) = \frac{P(t)}{V(t)} \quad [\mathrm{g}\cdot\mathrm{L}^{-1}], \quad r(t) = \frac{R(t)}{V(t)} \quad [\mathrm{g}\cdot\mathrm{L}^{-1}], \quad c(t) = \frac{C(t)}{V(t)} \quad [\mathrm{g}\cdot\mathrm{L}^{-1}],$$
$$m(t) = \frac{M(t)}{V(t)} = \frac{1}{\delta} - r(t) - c(t) \quad [\mathrm{g}\cdot\mathrm{L}^{-1}] \quad v_R(t) = \frac{V_R(t)}{V(t)} \quad [\mathrm{g}\cdot\mathrm{L}^{-1}\cdot\mathrm{h}^{-1}],$$
$$v_M(t) = \frac{V_M(t)}{V(t)} \quad [\mathrm{g}\cdot\mathrm{L}^{-1}\cdot\mathrm{h}^{-1}].$$

Using the relation in Eq. (2), we can rewrite it as:

$$m(t) = \frac{1}{\delta}(1 - r(t) - c(t)). \tag{3}$$

- The growth rate of the self-replicating system is

$$\mu(t) = \frac{1}{V(t)}\frac{dV(t)}{dt} = \delta[v_R f(c) + (\gamma_M - \gamma_R)r(t) + (\gamma_M - \gamma_C)c(t) - \frac{\gamma_M}{\delta}].$$

Now, after the modification as mentioned above, the proposed model (Eq. (1)) can be written as follows:

$$\begin{aligned}
\frac{dp}{dt} &= v_M - f(c)v_R - p\,\delta\left[v_R f(c) + (\gamma_M - \gamma_R)r(t) + (\gamma_M - \gamma_C)c(t) - \frac{\gamma_M}{\delta}\right],\\
\frac{dr}{dt} &= \alpha(1-\beta)f(c)v_R - \gamma_R r - r\,\delta\left[v_R f(c) + (\gamma_M - \gamma_R)r(t) + (\gamma_M - \gamma_C)c(t) - \frac{\gamma_M}{\delta}\right],\\
\frac{dc}{dt} &= \beta f(c)v_R - \gamma_C c - c\,\delta\left[v_R f(c) + (\gamma_M - \gamma_R)r(t) + (\gamma_M - \gamma_C)c(t) - \frac{\gamma_M}{\delta}\right],
\end{aligned} \tag{4}$$

where the dynamics of m is omitted, as it can be calculated directly from r and c according to relation (3).

Following the work of [13], the metabolic flux can be described as

$$v_M(t) = e_M\, m(t) = e_M\left(\frac{1}{\delta} - r(t) - c(t)\right), \tag{5}$$

where $e_M > 0$ $[\mathrm{h}^{-1}]$ represents the effective input from the environment, capturing the concentration and quality of external nutrients. It can be expressed in Michaelis-Menten form as

$$e_M(t) := k_M \frac{s(t)}{K_M + s(t)},$$

with $k_M > 0$ $[\mathrm{h}^{-1}]$ and $K_M > 0$ $[\mathrm{g} \cdot \mathrm{L}^{-1}]$ denoting the rate and half-saturation constants of metabolism and $s(t)$ the nutrient concentration in the medium. This approximation holds when $s(t) \approx \text{const}$ or $s(t) \gg K_M$. The translational flux is governed by the gene expression machinery and follows a Michaelis-Menten relation:

$$v_R(t) = k_R\, r(t)\, \frac{p(t)}{K_R + p(t)},$$

with $k_R > 0$ $[\mathrm{h}^{-1}]$ the catalytic rate constant and $K_R > 0$ $[\mathrm{g} \cdot \mathrm{L}^{-1}]$ the half-saturation constant. The modulation function gives the effective translation adjusted for the RNA-chaperone activity of CspA,

$$f(c) = 1 + \frac{\eta c^n}{k_c^n + c^n}, \tag{6}$$

where $c(t)$ is the intracellular CspA concentration, k_c $[\mathrm{g} \cdot \mathrm{L}^{-1}]$ the activation constant, η a folding-efficiency parameter, and n the Hill coefficient. Here $n = 2$ reflects CspA's experimentally observed cooperative binding to single-stranded RNA under cold-shock conditions [8]. The effective translational flux incorporating CspA activity is then $f(c)v_R(t)$.

Now, let us rescale the model to simplify its mathematical analysis. We introduce the following dimensionless variables and constants:

$$\hat{t} = k_R t, \quad \hat{p}(\hat{t}) = \delta\, p(t), \quad \hat{r}(\hat{t}) = \delta\, r(t), \quad \hat{m}(\hat{t}) = \delta\, m(t) \quad \hat{c}(\hat{t}) = \delta\, c(t)$$
$$E_M = \frac{e_M}{k_R}, \quad K = \delta\, K_R, \quad K_c = \delta\, k_c, \quad \Gamma_M = \frac{\gamma_M}{k_R}, \quad \Gamma_R = \frac{\gamma_R}{k_R} \quad \Gamma_C = \frac{\gamma_C}{k_R}.$$

Substituting the nondimensional variables into Eq. (2) yields

$$\hat{m}(\hat{t}) + \hat{r}(\hat{t}) + \hat{c}(\hat{t}) = 1. \tag{7}$$

The system expressed in terms of concentrations (Eq. (4)) can be transformed into a dimensionless form using the rescaled variables and constants:

$$\begin{aligned}
\frac{d\hat{p}}{d\hat{t}} &= E_M(1 - \hat{r}(t) - \hat{c}(t)) - \left(\frac{\hat{p}(t)\hat{r}(t)}{K + \hat{p}(t)}\right)\left(1 + \frac{\eta \hat{c}^2(t)}{K_c^2 + \hat{c}^2(t)}\right) \\
&\quad - \hat{p}(t)\left[\frac{\hat{p}(t)\hat{r}(t)}{K + \hat{p}(t)}\left(1 + \frac{\eta \hat{c}^2(t)}{K_c^2 + \hat{c}^2(t)}\right) + (\Gamma_M - \Gamma_R)\hat{r}(t) + (\Gamma_M - \Gamma_C)\hat{c}(t) - \Gamma_M\right], \\
\frac{d\hat{r}}{d\hat{t}} &= \alpha(1 - \beta)\left(\frac{\hat{p}(t)\hat{r}(t)}{K + \hat{p}(t)}\right)\left(1 + \frac{\eta \hat{c}^2(t)}{K_c^2 + c^2(t)}\right) - \Gamma_R \hat{r}(t) \\
&\quad - \hat{r}(t)\left[\frac{\hat{p}(t)\hat{r}(t)}{K + \hat{p}(t)}\left(1 + \frac{\eta \hat{c}^2(t)}{K_c^2 + \hat{c}^2(t)}\right) + (\Gamma_M - \Gamma_R)\hat{r}(t) + (\Gamma_M - \Gamma_C)\hat{c}(t) - \Gamma_M\right], \\
\frac{d\hat{c}}{d\hat{t}} &= \beta\left(\frac{\hat{p}(t)\hat{r}(t)}{K + \hat{p}(t)}\right)\left(1 + \frac{\eta \hat{c}^2(t)}{K_c^2 + \hat{c}^2(t)}\right) - \Gamma_C \hat{c}(t) \\
&\quad - \hat{c}(t)\left[\frac{\hat{p}(t)\hat{r}(t)}{K + \hat{p}(t)}\left(1 + \frac{\eta \hat{c}^2(t)}{K_c^2 + \hat{c}^2(t)}\right) + (\Gamma_M - \Gamma_R)\hat{r}(t) + (\Gamma_M - \Gamma_C)\hat{c}(t) - \Gamma_M\right],
\end{aligned} \tag{8}$$

with the initial conditions:

$$\hat{p}(0) = \hat{p}_0, \quad \hat{r}(0) = \hat{r}_0, \quad \hat{c}(0) = \hat{c}_0, \tag{9}$$

where

$$\hat{m}(\hat{t}) = 1 - \hat{r}(\hat{t}) - \hat{c}(\hat{t}), \tag{10}$$

and

$$\alpha(\hat{t}) \in [\alpha_{min}, \alpha_{max}] = [0,1], \quad \beta(\hat{t}) \in [\beta_{min}, \beta_{max}] = [0, 0.2], \quad \forall \hat{t} \in [0, \hat{T}].$$

In the scaled system (Eq. (8)), the dynamical expression of $\hat{m}$ is given by Eq. (10). It is also evident that the concentrations $\hat{m}$, $\hat{r}$, and $\hat{c}$ are constrained to the interval $[0,1]$ due to physical limitations imposed by the relation in Eq. (7).

2.1 Parameter Specification

To model bacterial growth and resource allocation under cold-shock conditions, we used kinetic parameters previously measured and validated at 37°C [13]. Because direct experimental data at 15°C are limited, most parameters were adjusted using the Q_{10} temperature coefficient, a standard approximation for accounting for temperature-dependent reaction rates in microbial physiology:

$$k(T) = k(T_{\text{ref}}) \cdot Q_{10}^{\frac{T - T_{\text{ref}}}{10}}, \qquad Q_{10} = 2.5, \quad T_{\text{ref}} = 37°\text{C}, \; T = 15°\text{C}.$$

This Q_{10}-based scaling is widely used to predict temperature effects on microbial and biological process rates [19]. Parameters derived in this manner preserve the relative ratios among reaction rates while accounting for the overall slowing of metabolic and translational processes under cold-shock conditions. Parameter values associated with CspA-related processes, such as translation efficiency and protein half-life, were taken directly from experimental measurements performed at 15°C in previously published studies. The main parameter values used in the model are summarized in Table 1.

Table 1: Model parameters used in the present study along with their values and corresponding literature references.

Quantity	Symbol	37°C	15°C	Reference
Protein synthesis rate	k_r	3.6 h^{-1}	0.479551 h^{-1}	[13]
Environmental input	e_M	3.6 h^{-1}	0.133209 h^{-1}	[13]
Metabolic degradation rate	γ_m	$\frac{\ln(2)}{20}$ h^{-1}	0.0012824 h^{-1}	[13]
Gene expression degradation rate	γ_r	$\frac{\ln(2)}{100}$ h^{-1}	0.000256481 h^{-1}	[13]
CspA degradation rate	γ_c	—	$\frac{\ln(2)}{20}$ h^{-1}	[8]
Inverse of cytoplasmic density	δ	0.003 [L·g^{-1}]	0.003 [L·g^{-1}]	[13]
Half-saturation constant	K_r	1 [g·L^{-1}]	1 [g·L^{-1}]	[13]
CspA translation efficiency	η	—	2	[8]
CspA half-saturation constant	k_c	—	0.7	[8]

3 Effects of Temperature

Since almost all the parameters of the proposed model (Eq. (4)) depend on the temperature of the environment. Therefore, we analyze the impact of different levels of temperature on the dynamics of the proposed model in this section.

3.1 Steady State Analysis

Following the resource allocation framework of Giordano et al. (2016), we determine the steady state

$$(\hat{p}^*_{\text{opt}}, \hat{r}^*_{\text{opt}}, \hat{c}^*_{\text{opt}}) \in G$$

of the system (Eq. (8)), at which the growth rate $\hat{\mu}$ attains its maximum. In contrast to approaches where analytical parameterizations of the steady state are available, here the nonlinearities in $f(\hat{c})$ and $\nu_R(\hat{p}, \hat{r})$ preclude closed-form solutions. To solve this system numerically, we employ a two-stage procedure. First, a coarse grid search is performed to identify promising regions in the parameter space (α, β). This is followed by a refined optimization using the global, derivative-free differential_evolution algorithm [20] from SciPy. Such numerical strategies are increasingly used in systems biology to overcome convergence issues associated with steady-state constraints [21].

The resulting optimal allocation at the reference temperature 15°C is

$$(\hat{p}^*_{\text{opt}}, \hat{r}^*_{\text{opt}}, \hat{c}^*_{\text{opt}}, \alpha_{\text{opt}}, \beta_{\text{opt}}) = (0.0121,\ 0.0560,\ 0.0056,\ 0.0559,\ 0.0088),$$

with an associated growth rate

$$\hat{\mu}^* = 0.122\,\text{h}^{-1}, \quad \text{corresponding to a doubling time } T_d = \frac{\ln 2}{\hat{\mu}^*} \approx 5.69\,\text{h}.$$

At this optimum, the proteome fractions are distributed as

$$\hat{r}^* : \hat{c}^* : \hat{m}^* = 5.6\% : 0.6\% : 93.8\%,$$

where $\hat{m}^* = 1 - \hat{r}^* - \hat{c}^*$ denotes the fraction of metabolic proteins. This indicates that only a small investment in CspA is sufficient to sustain growth, while the vast majority of resources remain allocated to metabolic functions under cold-shock conditions.

The convergence of the dynamical system towards the steady state shows that $\hat{p}(t)$, $\hat{r}(t)$, $\hat{c}(t)$, and $\hat{\mu}(t)$ approach their optimal values for the given initial conditions (Fig. 2). These simulations confirm that the numerically computed optimum corresponds to a stable equilibrium of the system and provide a quantitative baseline for the temperature and control analyses presented in the following sections.

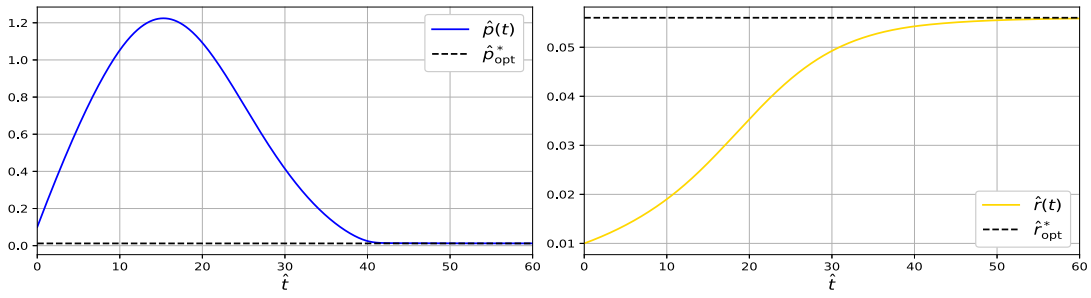

Figure 2: (Continued)

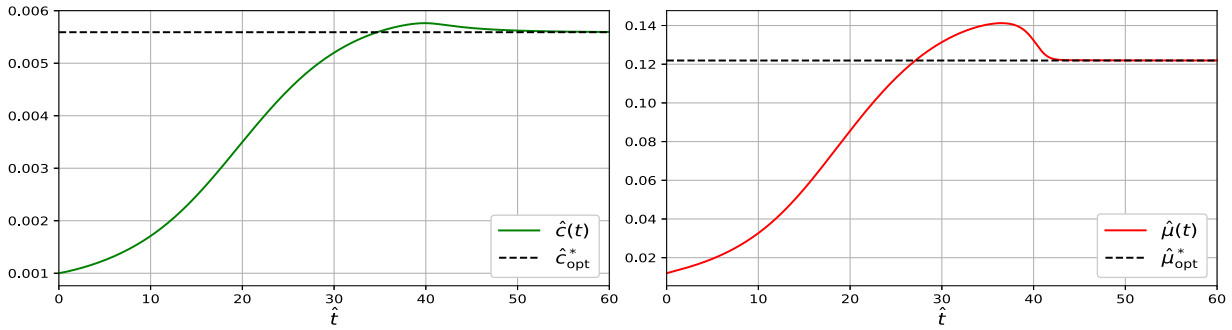

Figure 2: Simulation of the dynamical system showing convergence of $\hat{p}$, $\hat{r}$, $\hat{c}$ and $\hat{\mu}$ to their steady-state values at 15°C. The solid lines show the dynamical behavior of the proposed model, and the dotted lines show the respective steady states.

In addition to the reference case at 15°C, we computed the steady states for other temperatures (13°C, 17°C, and 19°C) using the same numerical procedure to validate our adopted technique. The resulting temperature-dependent steady-state values of $(\hat{p}^*, \hat{r}^*, \hat{c}^*, \alpha^*, \beta^*, \hat{\mu}^*)$ are summarized in Table 2 against each temperature. For each temperature, the associated dynamical simulations (see Figs. 3–5) show that $\hat{p}(t)$, $\hat{r}(t)$, $\hat{c}(t)$, and $\hat{\mu}(t)$ converges smoothly to their respective steady-state values listed in the Table 2. This behavior confirms that, at every temperature considered, the model admits a unique equilibrium toward which trajectories consistently converge.

Table 2: The steady-state values at the indicated temperatures.

T (°C)	$\hat{p}^*$	$\hat{r}^*$	$\hat{c}^*$	α^*	β^*	$\hat{\mu}^*$ (h^{-1})
13	0.011130	0.048777	0.005015	0.048637	0.009138	0.102342
15	0.012079	0.056021	0.005591	0.055893	0.008788	0.121907
17	0.013140	0.064585	0.006156	0.064473	0.008603	0.144955
19	0.014320	0.074627	0.006708	0.074539	0.008558	0.172023

At steady state across the analyzed temperature range (13°C–19°C), the model predicts relatively small CspA fractions. This is consistent with growth-optimized proteome allocation, in which CspA acts primarily as a regulatory component rather than a dominant protein species. While CspA can reach high abundance during acute cold shock, such levels reflect transient stress responses following rapid temperature downshift and are not representative of adapted steady-state growth. Under steady conditions, excessive CspA expression imposes translational and metabolic costs, leading cells to preferentially allocate resources toward ribosomal and metabolic proteins, resulting in a minimal-sufficient CspA level.

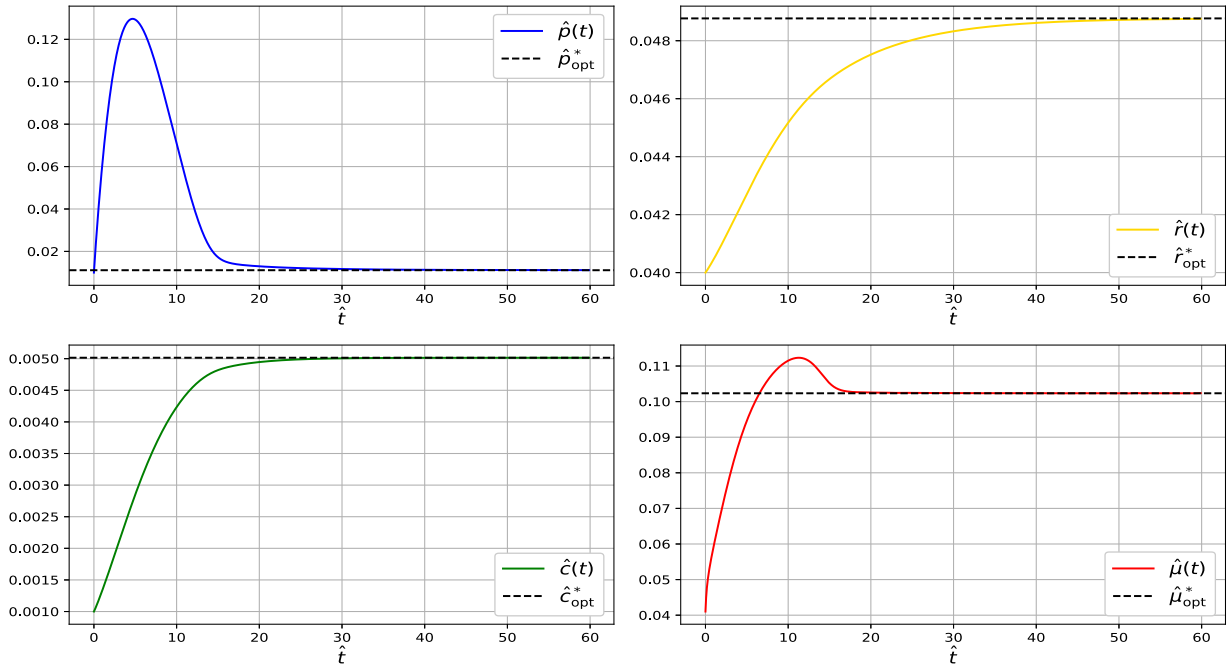

Figure 3: Simulation of the dynamical system showing convergence of $\hat{p}$, $\hat{r}$, $\hat{c}$ and $\hat{\mu}$ to their steady-state values at 13°C. The solid lines show the dynamical behavior of the proposed model, and the dotted lines show the respective steady states.

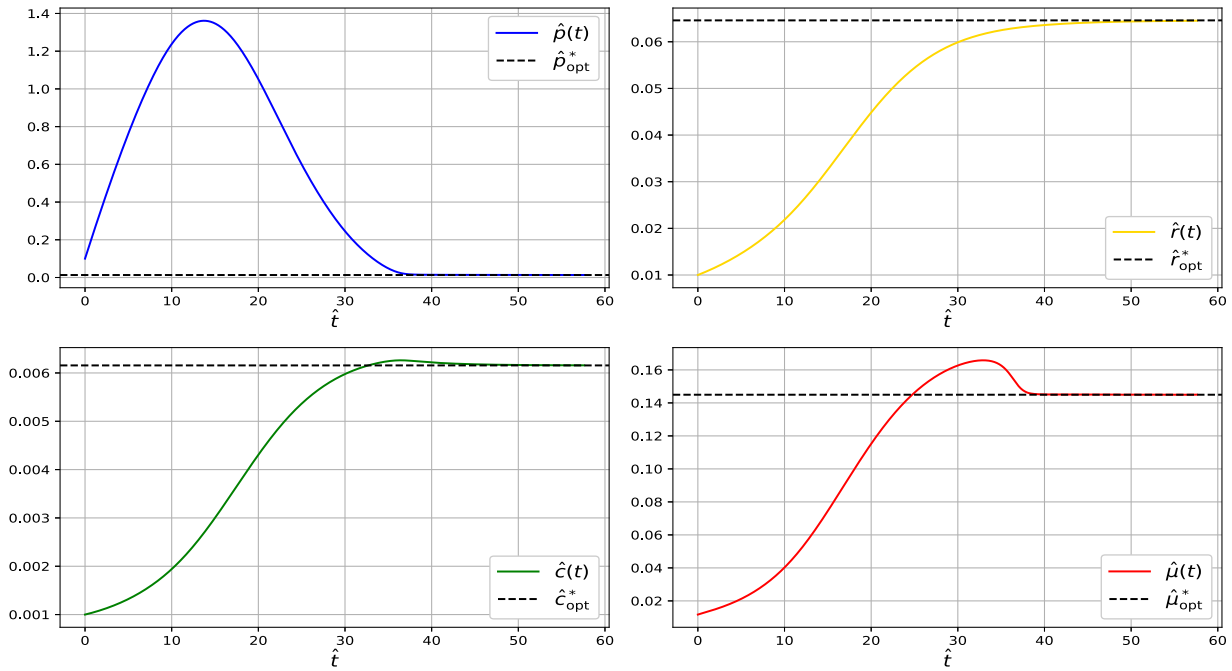

Figure 4: Simulation of the dynamical system showing convergence of $\hat{p}$, $\hat{r}$, $\hat{c}$ and $\hat{\mu}$ to their steady-state values at 17°C. The solid lines show the dynamical behavior of the proposed model, and the dotted lines show the respective steady states.

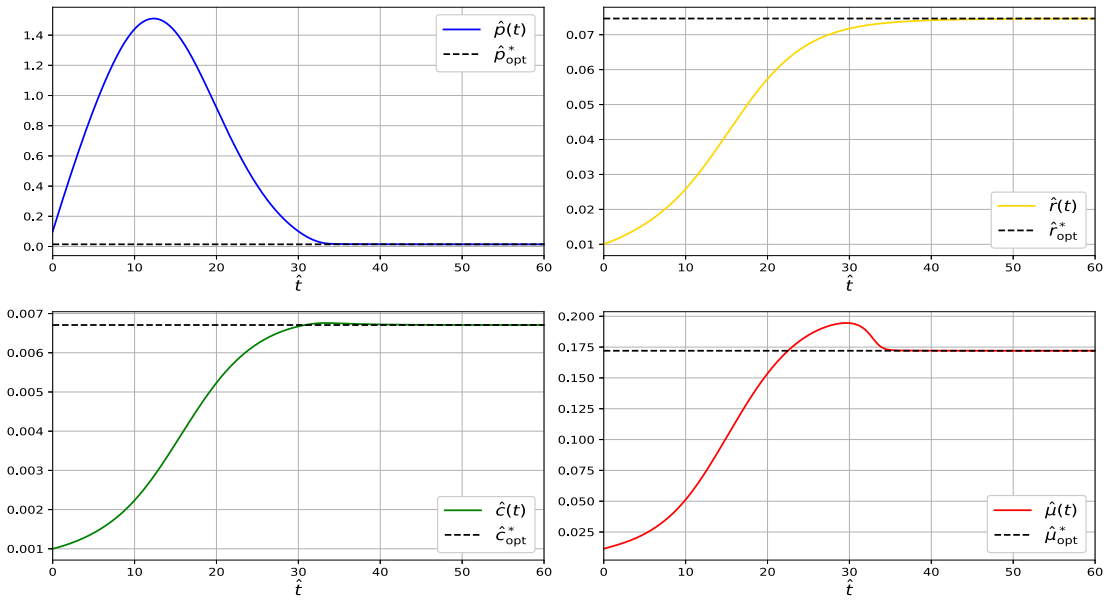

Figure 5: Simulation of the dynamical system showing convergence of $\hat{p}$, $\hat{r}$, $\hat{c}$ and $\hat{\mu}$ to their steady-state values at 19°C. The solid lines show the dynamical behavior of the proposed model, and the dotted lines show the respective steady states.

3.2 Stability Analysis

The local stability of a steady state of a dynamical system can be assessed using the Jacobian matrix approach [22].

Theorem 1: *A steady state is locally asymptotically stable if all the eigenvalues of the Jacobian matrix evaluated at the steady state have negative real parts.*

For system (8), the Jacobian matrix J is obtained by differentiating the right-hand side with respect to the state variables $(\hat{p}, \hat{r}, \hat{c})$. The resulting Jacobian matrix is shown below

$$J = \begin{pmatrix} -Af(\hat{c})(1+(\hat{p}^2+2\hat{p}K)) + B_1 & -e_m - \frac{\hat{p}(1+\hat{p})}{K+\hat{p}} f(\hat{c}) - \hat{p}(\Gamma_M - \Gamma_R) & -e_m - A_1 B(1+\hat{p}) - \hat{p}(\Gamma_M - \Gamma_C) \\ f(\hat{c})A(\alpha(1-\beta) - \hat{r}) & f(\hat{c})\frac{\hat{p}}{K+\hat{p}}(\alpha(1-\beta) - 2\hat{r}) - 2\hat{r}(\Gamma_M - \Gamma_R) - \Gamma_R & A_1 B(\alpha(1-\beta) - \hat{r}) - (\Gamma_M - \Gamma_C)\hat{r} \\ f(\hat{c})A(\beta - \hat{c}) & \frac{\hat{p}}{K+\hat{p}} f(\hat{c})(\beta - \hat{c}) - c(\Gamma_M - \Gamma_C) & \beta A_1 B - \Gamma_C - [\hat{c}B + f(\hat{c})]A_1 - B_1 - (\Gamma_M - \Gamma_C) \end{pmatrix}.$$

The Jacobian is evaluated at the steady state $(\hat{p}^*, \hat{r}^*, \hat{c}^*)$. where

$$A = \frac{\hat{r}K}{(K+\hat{p})^2}, \qquad A_1 = \frac{\hat{p}\hat{r}}{K+\hat{p}}, \qquad B = \frac{\eta K_c}{(K_c+\hat{c})^2}(\Gamma_M - \Gamma_R)\hat{r} + (\Gamma_M - \Gamma_C)\hat{c} - \Gamma_M.$$

Because of the strong nonlinearities, we compute the eigenvalues of the Jacobian matrix J numerically at each temperature's steady state. The results are reported in Table 3.

Across all temperatures examined (13°C–19°C), the Jacobian eigenvalues remain strictly negative, confirming that the steady state at each temperature is locally asymptotically stable. Together with the dynamical simulations (Figs. 2–5), which show that trajectories consistently converge to these steady states, the results demonstrate that the system reliably settles into its temperature-dependent equilibrium. This indicates that the qualitative stability properties of the model are preserved throughout the entire physiological temperature range analyzed.

Table 3: Eigenvalues of the Jacobian matrix B at each steady state for the corresponding temperature.

Temperature (°C)	λ_1	λ_2	λ_3
13	−2.45284	−0.24355	−0.31563
15	−2.45284	−0.24355	−0.31563
17	−2.24172	−0.14527	−0.20535
19	−2.30371	−0.17239	−0.22225

3.3 Steady-State Growth

We consider *E. coli* growth processes in the temperature range $T_0 \leq T \leq T_1$, where T_0 = 13°C (286.15 K) and T_1 = 19°C (292.15 K). One can see how the optimal dimensionless steady-state growth rate $\hat{\mu}^*_{\text{opt}}$ varies with temperature (Fig. 6). This temperature interval was selected to represent mild cold-acclimation conditions under which *E. coli* remains metabolically active and cold-shock regulation is functionally relevant. Within this range, temperature effects on metabolic and translational processes can be approximated using continuous scaling relationships such as Q_{10}. The applicability of model predictions outside this interval is limited: as temperature decreases below this range, growth becomes increasingly dominated by physical and survival constraints not captured by the present formulation, while as temperature increases beyond this range, cold-shock regulation progressively loses relevance and standard growth physiology dominates. For each temperature, the steady-state values of the allocation parameters and concentrations (α^*_{opt}, β^*_{opt}, p^*_{opt}, r^*_{opt}, c^*_{opt}) were determined numerically as those that maximize the growth rate. Because the effective growth time scale changes with temperature, growth rates computed at different temperatures are compared using the same dimensionless time variable $\hat{t}$, chosen here to correspond to 15°C. All parameter values used in these simulations are taken from Table 1, and temperature variation is applied according to the scaling based on Q_{10} described in the parameter specification section.

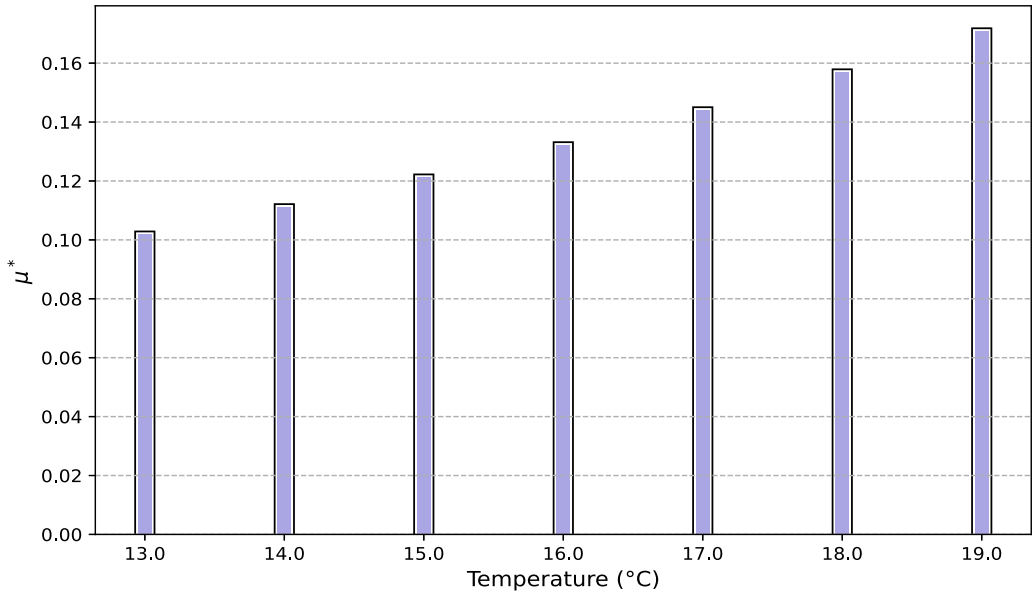

Figure 6: Temperature-dependent behavior of the optimal dimensionless steady-state growth rate $\hat{\mu}^*$ for parameters set in Table 1.

Next, we analyzed how bacterial growth depends on the allocation parameter β, which represents the fraction of cellular resources directed toward the synthesis of the cold-shock protein CspA. For each temperature, and for each fixed value of β, the remaining allocation parameter α and the concentrations p, r, and c were numerically optimized at steady state yielding $(\alpha^*_{\text{opt}}, p^*_{\text{opt}}, r^*_{\text{opt}}, c^*_{\text{opt}})$ to maximize the steady state growth. At low temperatures, moderate allocation to CspA enhances growth by improving translational efficiency through alleviation of inhibitory mRNA secondary structures. However, excessive allocation to CspA diverts translational resources away from ribosome synthesis and metabolic protein production, ultimately reducing the overall growth rate. Across the temperature range considered, the optimal value of β remains the same. Values of β higher than this optimum lead to reduced growth, highlighting the trade-off between stress protection and resource allocation for growth, and indicating that additional allocation to CspA offers no further benefit at higher temperatures and instead diverts resources away from ribosome and metabolic protein synthesis. The growth rate is maximized when β is set to its steady-state optimal value, β^*_{opt} (Fig. 7).

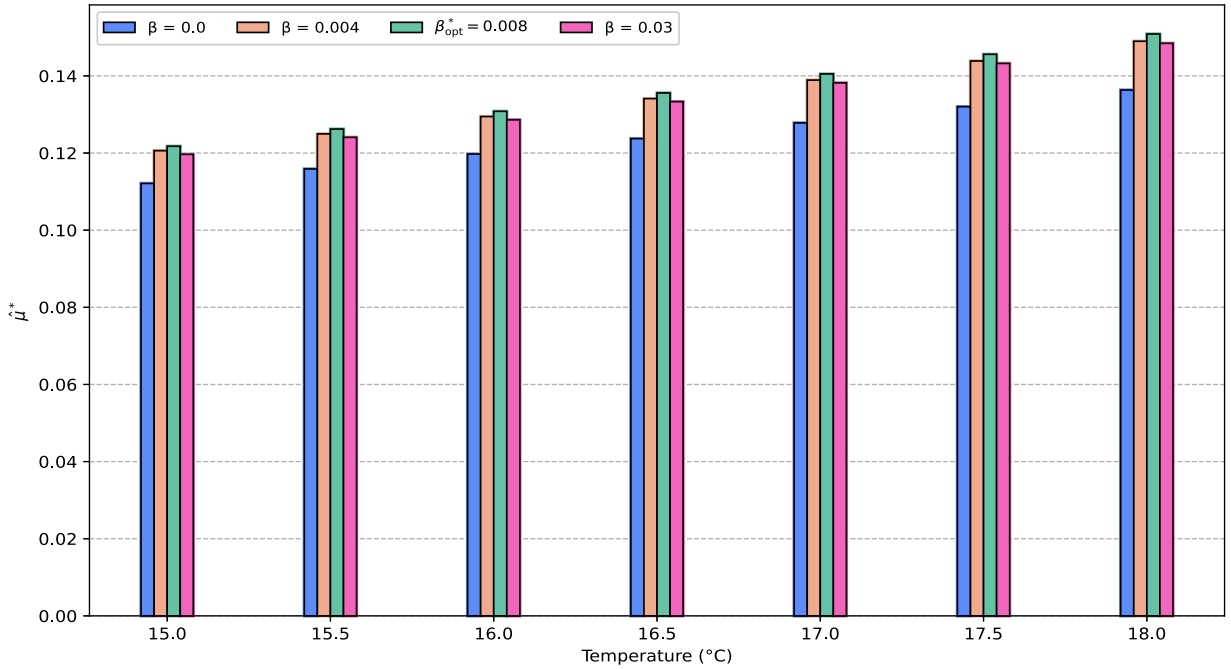

Figure 7: Effect of the control parameter β on the bacterial growth rate over the temperature range $T_0 = 15°C$ to $T_1 = 18°C$. For each value of β and at each temperature, the allocation parameter α and the concentrations $\hat{p}$, $\hat{r}$, and $\hat{c}$ were numerically optimized at steady state. The growth curve reaches its overall maximum when β takes the steady state optimal value, β^*_{opt}. Increasing β beyond this optimum reduces the growth rate across all temperatures, indicating that CspA contributes positively to growth only up to a certain level.

4 Optimal Control Problem

Optimal control theory provides a principled framework for quantifying how cells should allocate limited resources over time to maximize growth under environmental constraints [13,23–25]. In our setting, the control variables $\alpha(t)$ and $\beta(t)$ represent the fractions of translational capacity devoted to ribosome synthesis and CspA production. Applying Pontryagin's Maximum Principle yields the necessary optimality conditions and identifies candidate allocation strategies that balance biomass production with the costs of cold-shock adaptation. We formulate the optimal resource allocation problem for system (Eq. (8)) as the maximization of cumulative biomass production over the finite horizon $[0, \hat{T}]$. Following previous work [13],

we assume that *E. coli* regulates its proteome to maximize structural biomass under prevailing environmental conditions. This leads to the objective functional

$$J(\alpha(\hat{t}),\beta(\hat{t})) = \int_0^{\hat{T}} \mu(t)\,dt = \int_0^{\hat{T}} \hat{\mu}(\hat{t})\,dt \;\longrightarrow\; \max_{\alpha(\hat{t}),\beta(\hat{t})},$$

where

$$\hat{\mu}(\hat{t}) = \frac{\mu}{k_R} = \frac{\hat{p}(t)\,\hat{r}(t)}{K_R + \hat{p}(\hat{t})}\left(1 + \frac{\eta\hat{c}^2}{K_c^2 + \hat{c}^2}\right) + (\Gamma_M - \Gamma_R)\hat{r}(\hat{t}) + (\Gamma_M - \Gamma_C)\hat{c}(\hat{t}) - \Gamma_M,$$

which represents the cumulative biomass production over the time horizon $[0, \hat{T}]$. The optimization is carried out over all measurable open-loop control functions $\alpha(\hat{t})$ and $\beta(\hat{t})$.

We assume that environmental variations, such as nutrient upshifts or downshifts, occur as instantaneous shifts [13]. For example, *Escherichia coli* transitions rapidly between habitats such as the mammalian gut, water bodies, soils, and sediments, where intermediate fluctuations are negligible. Each shift specifies a new value of the environmental input e_M, defining a distinct optimal allocation problem. Between two consecutive shifts, e_M is treated as constant, representing bacterial adaptation over the finite interval between environmental changes.

Earlier studies formulated growth maximization as an infinite-horizon problem under the overtaking optimality criterion, implicitly assuming that trajectories reach and remain at the steady state corresponding to maximum growth rate. However, the formal existence of such overtaking optimal strategies was not proven, and infinite-horizon problems cannot be solved numerically. Finite-horizon simulations with free terminal states revealed small deviations from steady state near the end of the interval, regarded as artifacts under turnpike theory [26].

Following the approach of Yegorov et al. (2018) [13], we therefore consider two finite-horizon formulations: (i) without a terminal condition, where the final state is free, and (ii) with a fixed terminal condition, constraining the state variables to reach the steady state corresponding to maximum growth:

$$(p(\hat{T}), r(\hat{T}), c(\hat{T})) = (\hat{p}^*_{\text{opt}}, \hat{r}^*_{\text{opt}}, \hat{c}^*_{\text{opt}}), \qquad \hat{T} \in (0, +\infty). \tag{11}$$

4.1 Optimality Conditions

In optimal control theory, Pontryagin's Maximum Principle (PMP) [27,28] provides the first-order necessary conditions for open-loop control strategies. The PMP has been used extensively in microbial resource-allocation models [9,13,22] and is well suited for the present problem, where the controls $\alpha(t)$ and $\beta(t)$ govern translational allocation to ribosomes and CspA. For our proposed model (Eq. (8)), the application of PMP yields necessary conditions consisting of the Hamiltonian, adjoint system, and optimality conditions, as summarized below. The Hamiltonian is defined as

$$\begin{aligned} H(\hat{p},\hat{r},\hat{c},\alpha,\beta,\lambda_0,\lambda_p,\lambda_r,\lambda_c) = {} & \lambda_p\Bigg[E_M(1-\hat{r}-\hat{c}) - f(\hat{c})\left(\frac{\hat{p}\hat{r}}{K+\hat{p}}\right) \\ & - \hat{p}\Big(f(\hat{c})\left(\frac{\hat{p}\hat{r}}{K+\hat{p}}\right) + (\Gamma_M-\Gamma_R)\hat{r} + (\Gamma_M-\Gamma_C)\hat{c} - \Gamma_M\Big)\Bigg] \\ & + \lambda_r\Bigg[\alpha(1-\beta)f(\hat{c})\left(\frac{\hat{p}\hat{r}}{K+\hat{p}}\right) - \Gamma_R\hat{r} - \hat{r}\Big(f(\hat{c})\left(\frac{\hat{p}\hat{r}}{K+\hat{p}}\right) \end{aligned}$$

$$
\begin{aligned}
&+ (\Gamma_M - \Gamma_R)\hat{r} + (\Gamma_M - \Gamma_C)\hat{c} - \Gamma_M\Big)\Bigg] \\
&+ \lambda_c\Bigg[\beta f(\hat{c})\left(\frac{\hat{p}\hat{r}}{K+\hat{p}}\right) - \Gamma_C\hat{c} - \hat{c}\Big(f(\hat{c})\left(\frac{\hat{p}\hat{r}}{K+\hat{p}}\right) + (\Gamma_M - \Gamma_R)\hat{r} \\
&+ (\Gamma_M - \Gamma_C)\hat{c} - \Gamma_M\Big)\Bigg] + \lambda_0\Bigg[f(\hat{c})\left(\frac{\hat{p}\hat{r}}{K+\hat{p}}\right) + (\Gamma_M - \Gamma_R)\hat{r} \\
&+ (\Gamma_M - \Gamma_C)\hat{c} - \Gamma_M\Bigg],
\end{aligned} \tag{12}
$$

where $\hat{p}$, $\hat{r}$, and $\hat{c}$ denote the non-dimensionalized state variables, λ_p, λ_r, and λ_c are the adjoint variables, and α, β are the time-dependent control variables. From Pontryagin's Maximum Principle, the adjoint variables satisfy

$$
\frac{d\lambda_j}{d\hat{t}} = -\frac{\partial H}{\partial y_j}, \quad j = 1, 2, 3, \tag{13}
$$

which yields the following adjoint equations:

$$
\begin{aligned}
\frac{d\lambda_p}{d\hat{t}} =& \frac{K\hat{r}}{K+\hat{p}} f(c)\left(\lambda_p(1+\hat{p}+\lambda_r(\hat{r}-(1-\beta)\alpha)+\lambda_c(\hat{c}-\beta)+\lambda_0\right) \\
&+ \lambda_p\left(\frac{\hat{p}\hat{r}}{K+\hat{p}} f(\hat{c}) + (\Gamma_M - \Gamma_R)\hat{r} + (\Gamma_M - \Gamma_C)\hat{c} - \Gamma_M\right), \\
\frac{d\lambda_r}{d\hat{t}} =& \lambda_p E_M + \frac{\hat{p}}{K+\hat{p}} f(\hat{c})\left(\lambda_p(1+\hat{p}+\lambda_r(2\hat{r}-(1-\beta)\alpha)+\lambda_c(\hat{c}-\beta)+\lambda_0\right) \\
&+ (\Gamma_M - \Gamma_R)\left(\lambda_p\hat{p} + \lambda_r(2\hat{r}-1) + \lambda_c\hat{c} + \lambda_0\right) + (\Gamma_M - \Gamma_C)\lambda_c\hat{c}, \\
\frac{d\lambda_c}{d\hat{t}} =& \lambda_p E_M + \frac{\hat{p}\hat{r}}{K+\hat{p}} f'(\hat{c})\left(\lambda_p(1+\hat{p}+\lambda_r(\hat{r}-(1-\beta)\alpha)+\lambda_c(\hat{c}-\beta)+\lambda_0\right) \\
&+ (\Gamma_M - \Gamma_C)\left(\lambda_p\hat{p} + \lambda_r\hat{r} - + \lambda_c(2\hat{c}-1) + \lambda_0\right) + \lambda_c\left(\frac{\hat{p}\hat{r}}{K+\hat{p}} f(\hat{c}) + (\Gamma_M - \Gamma_C)\hat{r}\right)
\end{aligned} \tag{14}
$$

where

$$
f(\hat{c}) = \left(1 + \frac{\eta\hat{c}^2}{K_c^2 + \hat{c}^2}\right), \qquad f'(\hat{c}) = \frac{2\eta\hat{c}K_c^2}{(K_c^2 + \hat{c}^2)^2},
$$

$$
\lambda_0 \equiv 0 \ \text{ or } \ \lambda_0 \equiv -1,
$$

$$
(\lambda_0, \lambda_p(\hat{t}), \lambda_r(\hat{t}), \lambda_c(\hat{t})) \neq (0,0,0,0), \quad \forall\, \hat{t} \in [0, \hat{T}].
$$

The Hamiltonian maximum conditions are

$$
S_\alpha(\hat{t}) := \frac{\partial H}{\partial \alpha} = \lambda_r(\hat{t})(1-\beta(\hat{t}))\, f(\hat{c})\, \frac{\hat{p}(\hat{t})\hat{r}(\hat{t})}{K+\hat{p}(\hat{t})},
$$

$$
S_\beta(\hat{t}) := \frac{\partial H}{\partial \beta} = f(\hat{c})\, \frac{\hat{p}(\hat{t})\hat{r}(\hat{t})}{K+\hat{p}(\hat{t})}\, (\lambda_c(\hat{t}) - \alpha(\hat{t})\lambda_r(\hat{t})).
$$

where the optimal controls $\alpha(t)$ and $\beta(t)$ are given by

$$\alpha(\hat{t}) = \begin{cases} \alpha_{min}, & \text{if} \quad \lambda_r(\hat{t}) < 0, \\ \alpha_{max}, & \text{if} \quad \lambda_r(\hat{t}) > 0, \\ \alpha_{\mathbf{sing}}, & \text{if} \quad \lambda_r(\hat{t}) = 0, \end{cases}$$

$$\beta(\hat{t}) = \begin{cases} \beta_{min}, & \text{if} \quad \lambda_c(\hat{t}) - \alpha(\hat{t})\lambda_r(\hat{t}) < 0, \\ \beta_{max}, & \text{if} \quad \lambda_c(\hat{t}) - \alpha(\hat{t})\lambda_r(\hat{t}) > 0, \\ \beta_{\mathbf{sing}}, & \text{if} \quad \lambda_c(\hat{t}) - \alpha(\hat{t})\lambda_r(\hat{t}) = 0, \end{cases}$$

which is a necessary condition for an optimal open-loop control. An admissible process

$$\alpha(\hat{t}),\ \beta(\hat{t}),\ \hat{p}(\hat{t}),\ \hat{r}(\hat{t}),\ \hat{c}(\hat{t}),\ \lambda_0,\ \lambda_p(\hat{t}),\ \lambda_r(\hat{t}),\ \lambda_c(\hat{t})$$

that satisfies PMP conditions is called extremal. It is called normal if $\lambda_0 < 0$ and abnormal if $\lambda_0 = 0$. Since the controlled system is autonomous, that is, the right-hand sides of the state equations depend on time only through the state and control variables, the Hamiltonian is conserved along any extremal process.

If a switching function $S_\alpha(\hat{t})$ or $S_\beta(\hat{t})$ vanishes over some time subinterval, then the corresponding control $\alpha(\hat{t})$ or $\beta(\hat{t})$ is singular, and the associated trajectory lies on the singular manifold of the system. We now examine the structure of singular arcs arising from these switching functions

Theorem 2 ([23]): *Any singular arc $u_s(t)$ of a normal extremal solution of (OCP) is of at least second order.*

Proof: Assume that the process (φ, λ, u) satisfies the Pontryagin Maximum Principle (PMP) as a normal extremal, and set $\lambda_0 = -1$. To describe the singular arcs, suppose the switching functions vanish on a subinterval $\tau = [\hat{t}_1, \hat{t}_2] \subset [0, \hat{T}]$. The switching surfaces are defined by

$$\Sigma_\alpha = \{(\varphi, \lambda) \in \mathbb{R}^{2n} \mid S_\alpha = 0\}, \qquad \Sigma_\beta = \{(\varphi, \lambda) \in \mathbb{R}^{2n} \mid S_\beta = 0\},$$

where n is the number of state variables.

On the singular arc for α, $S_\alpha = 0$ implies $\lambda_r = 0$ (under the assumptions $\beta \neq 1$ and $\phi(\hat{p}, \hat{r}, \hat{c}) \neq 0$). Similarly, for β, $S_\beta = 0$ implies $\lambda_c = \alpha\lambda_r$. If both controls are singular, then $\lambda_r = 0$ and $\lambda_c = 0$. Here we define

$$\phi(\hat{p}, \hat{r}, \hat{c}) = f(\hat{c})\, \frac{\hat{p}\hat{r}}{K + \hat{p}},$$

as a convenient shorthand for the product term appearing in the switching functions. To compute the derivatives of the switching functions, we use the Poisson bracket operator

$$\{f, g\} = \sum_{i=1}^{n} \left(\frac{\partial f}{\partial \lambda_i} \frac{\partial g}{\partial \varphi_i} - \frac{\partial f}{\partial \varphi_i} \frac{\partial g}{\partial \lambda_i} \right), \tag{15}$$

where φ_i are the state variables and λ_i are the costate variables. For simplicity, we write the switching functions as

$$S_\alpha(\hat{t}) := \frac{\partial H}{\partial \alpha} = \phi(\hat{p}, \hat{r}, \hat{c})(1 - \beta)\, \lambda_r,$$

$$S_\beta(\hat{t}) := \frac{\partial H}{\partial \beta} = \phi(\hat{p}, \hat{r}, \hat{c})\, (\lambda_c - \alpha\lambda_r).$$

The first derivatives are

$$\dot{S}_\alpha = \dot{\lambda}_r(1-\beta)\,\phi(\hat{p},\hat{r},\hat{c}) + \lambda_r\Big[(1-\beta)\big(\phi_{\hat{p}}(\hat{p},\hat{r},\hat{c}) + \phi_{\hat{r}}(\hat{p},\hat{r},\hat{c}) + \phi_{\hat{c}}(\hat{p},\hat{r},\hat{c})\big) - \phi(\hat{p},\hat{r},\hat{c})\,\dot{\beta}\Big],$$

$$\begin{aligned}\dot{S}_\beta = {} & (\dot{\lambda}_c - \alpha\,\dot{\lambda}_r - \dot{\alpha}\lambda_r)(1-\beta)\,\phi(\hat{p},\hat{r},\hat{c}) \\ & + (\lambda_c - \alpha\lambda_r)\Big[(1-\beta)\big(\phi_{\hat{p}}(\hat{p},\hat{r},\hat{c}) + \phi_{\hat{r}}(\hat{p},\hat{r},\hat{c}) + \phi_{\hat{c}}(\hat{p},\hat{r},\hat{c})\big) - \phi(\hat{p},\hat{r},\hat{c})\dot{\beta}\Big],\end{aligned}$$

where

$$\phi_{\hat{p}}(\hat{p},\hat{r},\hat{c}) = \frac{\partial\phi(\hat{p},\hat{r},\hat{c})}{\partial\hat{p}}\dot{\hat{p}}, \qquad \phi_{\hat{r}}(\hat{p},\hat{r},\hat{c}) = \frac{\partial\phi(\hat{p},\hat{r},\hat{c})}{\partial\hat{r}}\dot{\hat{r}}, \qquad \phi_{\hat{c}}(\hat{p},\hat{r},\hat{c}) = \frac{\partial\phi(\hat{p},\hat{r},\hat{c})}{\partial\hat{c}}\dot{\hat{c}}.$$

Along the singular arc, the first derivatives vanish identically, implying that $\dot{\lambda}_r = 0$ and $\dot{\lambda}_c = 0$. As the Poisson bracket method does not directly resolve this case with two singular controls, we examined the second derivatives $\ddot{S}_\alpha$ and $\ddot{S}_\beta$ by evaluating them on $(S_\alpha, \dot{S}_\alpha)$ and $(S_\beta, \dot{S}_\beta)$, respectively, using SageMath. The controls α and β do not appear in these second derivatives, confirming that the singular arc is of at least second order.

Now consider α as the sole control while β is fixed. The first derivative is

$$\dot{S}_\alpha = \dot{\lambda}_r(1-\beta)\,\phi(\hat{p},\hat{r},\hat{c}) + \lambda_r(1-\beta)\big(\phi_{\hat{p}}(\hat{p},\hat{r},\hat{c}) + \phi_r(\hat{p},\hat{r},\hat{c}) + \phi_c(\hat{p},\hat{r},\hat{c})\big),$$

which vanishes identically along the singular arc. To compute higher-order derivatives of S_α, we employ the Poisson bracket operator [29]. The Hamiltonian can be expressed as

$$H = H_0 + \alpha H_1, \qquad H_1 = S_\alpha.$$

Applying this, we find

$$\dot{H}_1 = \frac{\partial H_1}{\partial\varphi}\dot{\varphi} + \frac{\partial H_1}{\partial\lambda}\dot{\lambda} = \sum_{i=1}^{n}\left(\frac{\partial H}{\partial\lambda_i}\frac{\partial H_1}{\partial\varphi_i} - \frac{\partial H}{\partial\varphi_i}\frac{\partial H_1}{\partial\lambda_i}\right) = \{H, H_1\} = \{H_0 + \alpha H_1, H_1\} = H_{01},$$

since $\{\alpha H_1, H_1\} = \alpha\{H_1, H_1\} = 0$. The second derivative is then

$$\ddot{H}_1 = \dot{H}_{01} = \{H_0, H_{01}\} + \alpha\{H_1, H_{01}\} = H_{001} + \alpha H_{101}.$$

To ensure the singular arc is at least of order two, we must show $H_{101} = 0$ along the switching surface Σ_α. Otherwise, a first-order singular control could be computed as $u = -H_{001}/H_{101}$. Because H_i depends only on $\lambda_r, \hat{p}, \hat{r}, \hat{c}$, the Poisson bracket becomes

$$\begin{aligned}H_{101} = \{H_1, H_{01}\} = {} & \frac{\partial H_1}{\partial\hat{p}}\frac{\partial H_{01}}{\partial\lambda_p} - \frac{\partial H_1}{\partial\lambda_p}\frac{\partial H_{01}}{\partial\hat{p}} + \frac{\partial H_1}{\partial\hat{r}}\frac{\partial H_{01}}{\partial\lambda_r} - \frac{\partial H_1}{\partial\lambda_r}\frac{\partial H_{01}}{\partial\hat{r}} + \frac{\partial H_1}{\partial\hat{c}}\frac{\partial H_{01}}{\partial\lambda_c} - \frac{\partial H_1}{\partial\lambda_c}\frac{\partial H_{01}}{\partial\hat{c}}, \\ = {} & \mu(\hat{p},\hat{r},\hat{c})\frac{\partial H_{01}}{\partial\lambda_r} - \lambda_r\mu_r(\hat{p},\hat{r},\hat{c})\frac{\partial H_{01}}{\partial\hat{r}} - \lambda_r\mu_p(\hat{p},\hat{r},\hat{c})\frac{\partial H_{01}}{\partial\hat{p}} - \lambda_r\mu_c(\hat{p},\hat{r},\hat{c})\frac{\partial H_{01}}{\partial\hat{c}},\end{aligned}$$

where

$$\frac{\partial H_{01}}{\partial\hat{r}} = \dot{\lambda}_r\phi_{\hat{r}}(\hat{p},\hat{r},\hat{c}) + \lambda_r\frac{\partial}{\partial\hat{r}}\big(\phi_{\hat{p}}(\hat{p},\hat{r},\hat{c})\dot{\hat{p}} + \phi_{\hat{r}}(\hat{p},\hat{r},\hat{c})\dot{\hat{r}} + \phi_{\hat{c}}(\hat{p},\hat{r},\hat{c})\dot{\hat{c}}\big).$$

Substituting this expression into the previous equation yields

$$H_{101} = \phi(\hat{p},\hat{r},\hat{c})\Big[\dot{\lambda}_r\phi_{\hat{r}}(\hat{p},\hat{r},\hat{c}) + \lambda_r\frac{\partial}{\partial r}\big(\phi_{\hat{p}}(\hat{p},\hat{r},\hat{c})\dot{p} + \phi_{\hat{r}}(\hat{p},\hat{r},\hat{c})\dot{r} + \phi_{\hat{c}}(\hat{p},\hat{r},\hat{c})\dot{c}\big)\Big] - \lambda_r\phi_{\hat{r}}(\hat{p},\hat{r},\hat{c})\frac{\partial H_{01}}{\partial \hat{r}}$$
$$- \lambda_r\phi_{\hat{p}}(\hat{p},\hat{r},\hat{c})\frac{\partial H_{01}}{\partial \hat{p}} - \lambda_r\phi_{\hat{c}}(\hat{p},\hat{r},\hat{c})\frac{\partial H_{01}}{\partial \hat{c}},$$

which equals zero along the switching surface since every term contains either λ_r or $\dot{\lambda}_r$, both identically zero on a singular arc. A completely analogous argument applies when α is fixed and β is the only control. Therefore, in all cases, the singular arc is of at least second order. Therefore, all singular arcs are of order at least two, and by standard results in geometric optimal control theory, arcs of order 2 cannot persist indefinitely but must enter and exit the singular region through chattering [27]. □

4.2 Simulation Results

Numerical simulations of the optimal control problem were performed using the `CasADi` library in Python, employing the `IPOPT` solver with a relative tolerance of 10^{-12}, a maximum of 100,000 iterations, and 1500 discretization steps with a time step of $\Delta t = 0.028$, corresponding to a total scaled horizon of $\hat{T} \approx 42$. Parameter values were taken from Table 1, and the initial conditions were set to $\hat{p}_0 = 0.01$, $\hat{r}_0 = 0.04$, and $\hat{c}_0 = 0.002$. The Crank–Nicolson scheme was used to discretize the system of ODEs over the finite time horizon, and the resulting nonlinear program was solved directly with `IPOPT`.

For the free-final-state formulation (without terminal constraints), numerical simulations show that all state variables converge to their steady-state values $(\hat{p}^*_{\text{opt}}, \hat{r}^*_{\text{opt}}, \hat{c}^*_{\text{opt}})$, while both controls α and β exhibit a characteristic bang–bang–singular behavior. Initially, the controls operate in bang-bang mode, rapidly switching between extreme values to adjust resource allocation. Through chattering, they enter the singular region, where they remain close to the steady-state optimal allocation values identified in the steady-state analysis. Over sufficiently long simulation times, the singular controls converge numerically to constant values, effectively holding the system at a steady state. This reflects a turnpike-like phenomenon [26], whereby the optimal dynamic trajectory spends most of the horizon near the steady-state configuration before deviating only near the boundaries. The corresponding state and control trajectories for the scenario without a terminal condition (Fig. 8) and the associated switching functions are also determined (Fig. 9). The accumulated growth (objective functional) initially increases slowly and then rises steadily as the system approaches the singular phase, reflecting efficient resource allocation over time.

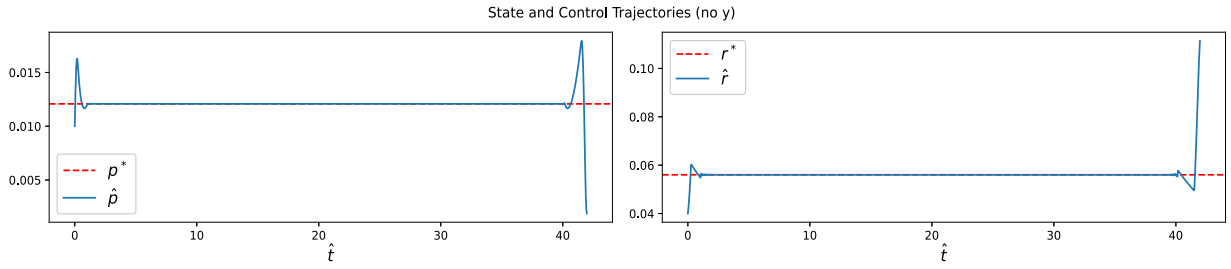

Figure 8: (Continued)

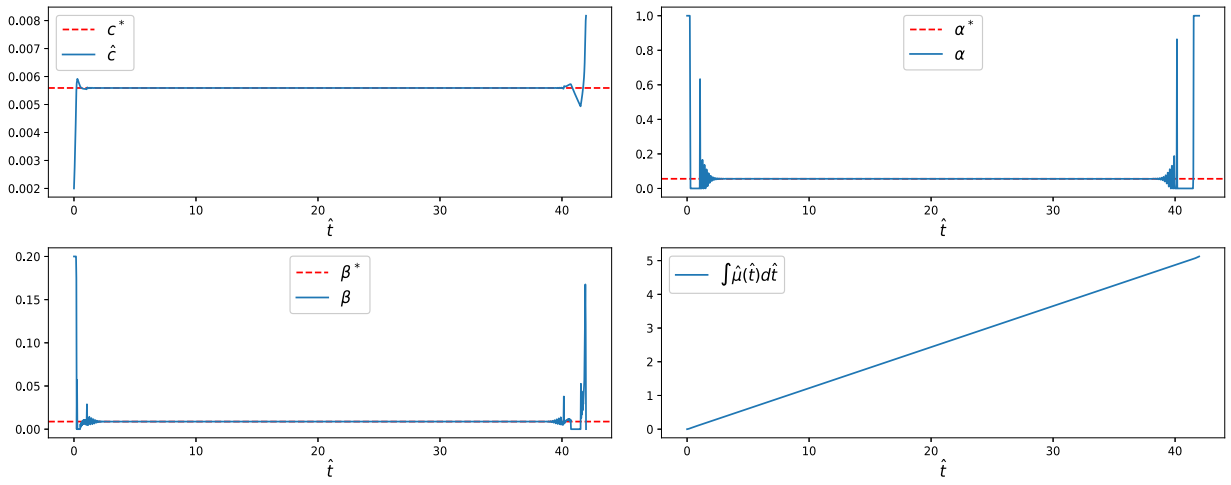

Figure 8: State and control trajectories for without a terminal condition. The dotted lines represent the steady-state optimal values, while the solid lines show the optimal trajectories. Both controls, α and β, exhibit bang–bang–singular behavior, entering and exiting the singular region via chattering, with the system near a steady state during the singular phase.

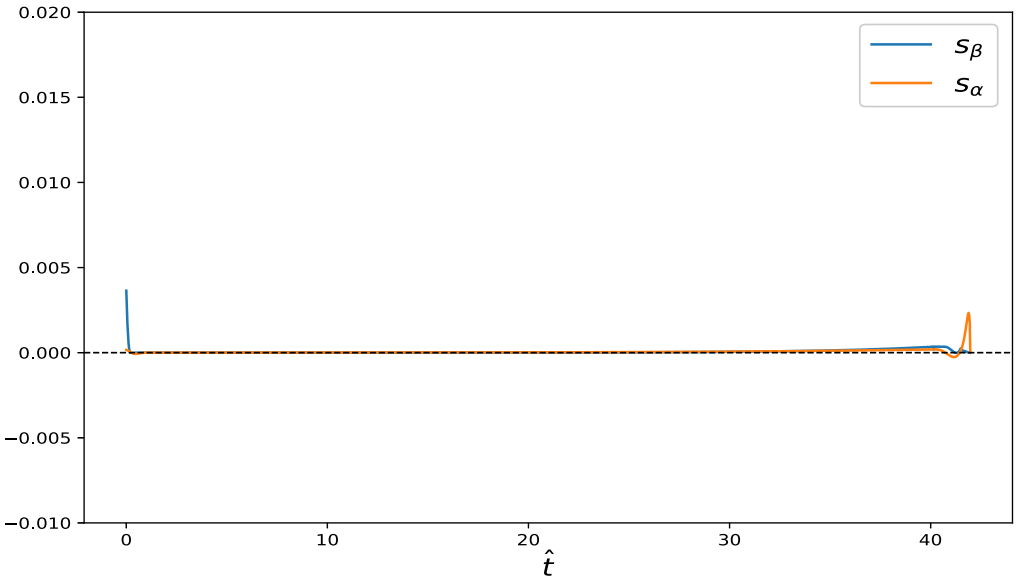

Figure 9: Switching functions S_α and S_β without terminal condition. Zero values indicate the singular phase, marking intervals where the system enters the singular regime.

We further examined two specific cases in the free-final-state setting: (i) β fixed at its steady-state optimal value with α as the only control (Figs. 10 and 11), and (ii) α fixed at its steady-state optimal value with β as the only control (Figs. 12 and 13). In both scenarios, the variable control enters the singular region and remains numerically at the steady-state optimal allocation during the singular phase. The corresponding state and control trajectories (Figs. 10 and 12) as well as the associated switching functions, are determined (Figs. 11 and 13). The switching functions remain zero while in the singular region, confirming that the controls maintain the optimal steady-state values during this interval. The accumulated growth in these

single-control cases shows similar trends, with a gradual increase before reaching a near-steady rate during the singular phase.

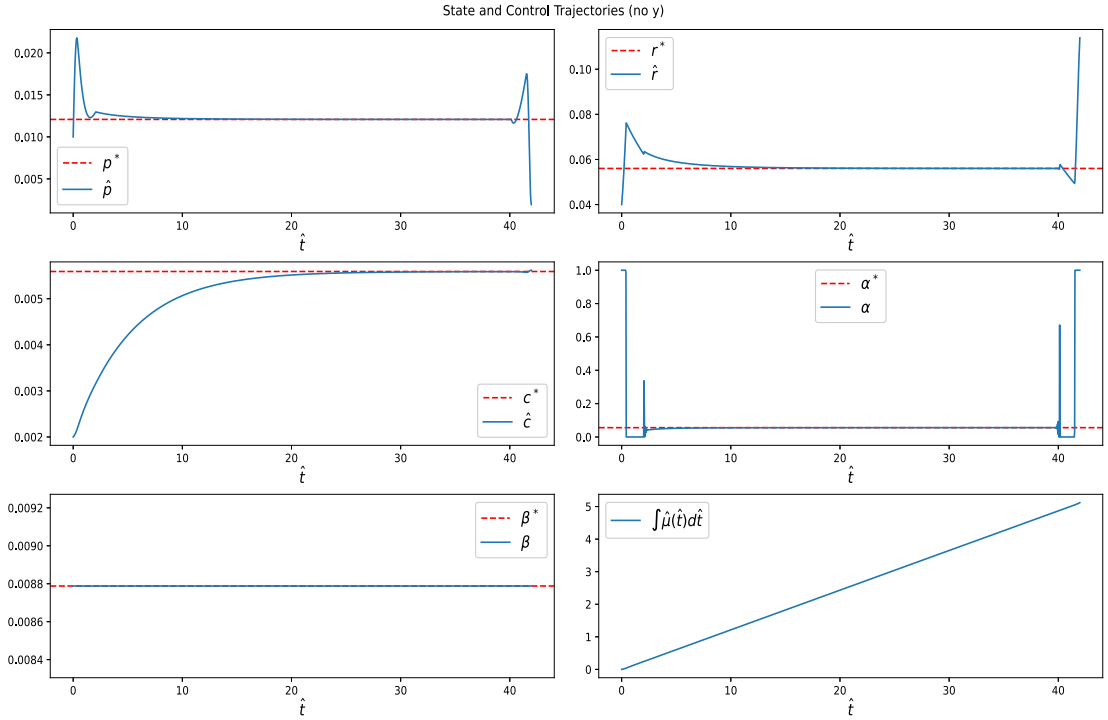

Figure 10: State variables and control input α for simulations with β fixed at its optimal steady-state optimal value. The dotted lines represent the steady-state values, while the solid lines show the optimal trajectories. Control α exhibits bang–bang–singular behavior, entering the singular region via chattering and remaining near the steady-state allocation during the singular phase and leaving it near the end.

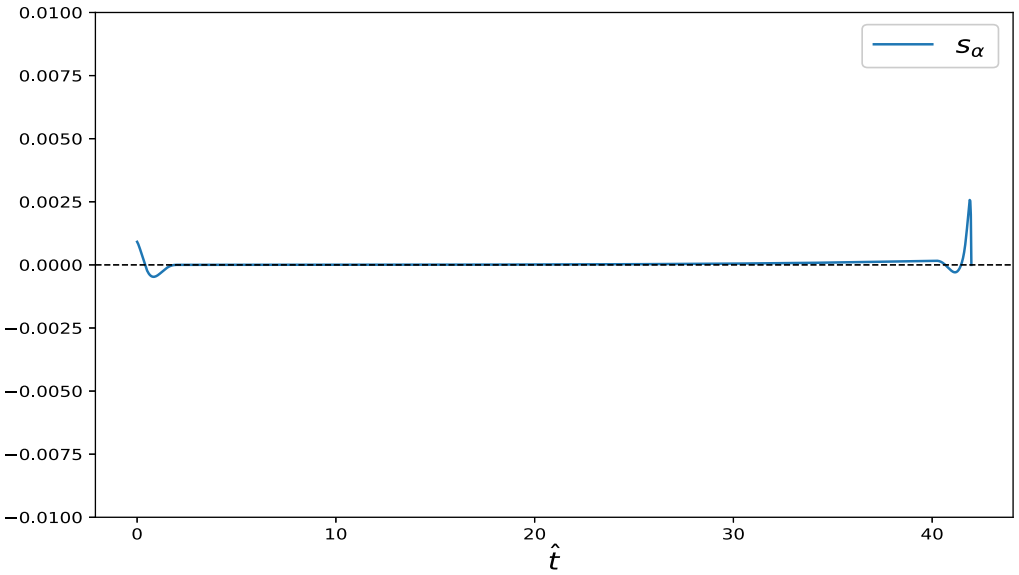

Figure 11: Switching function S_α for the scenario with β fixed at its optimal steady-state value. Zero values indicate the singular phase, showing intervals where α enters the singular regime.

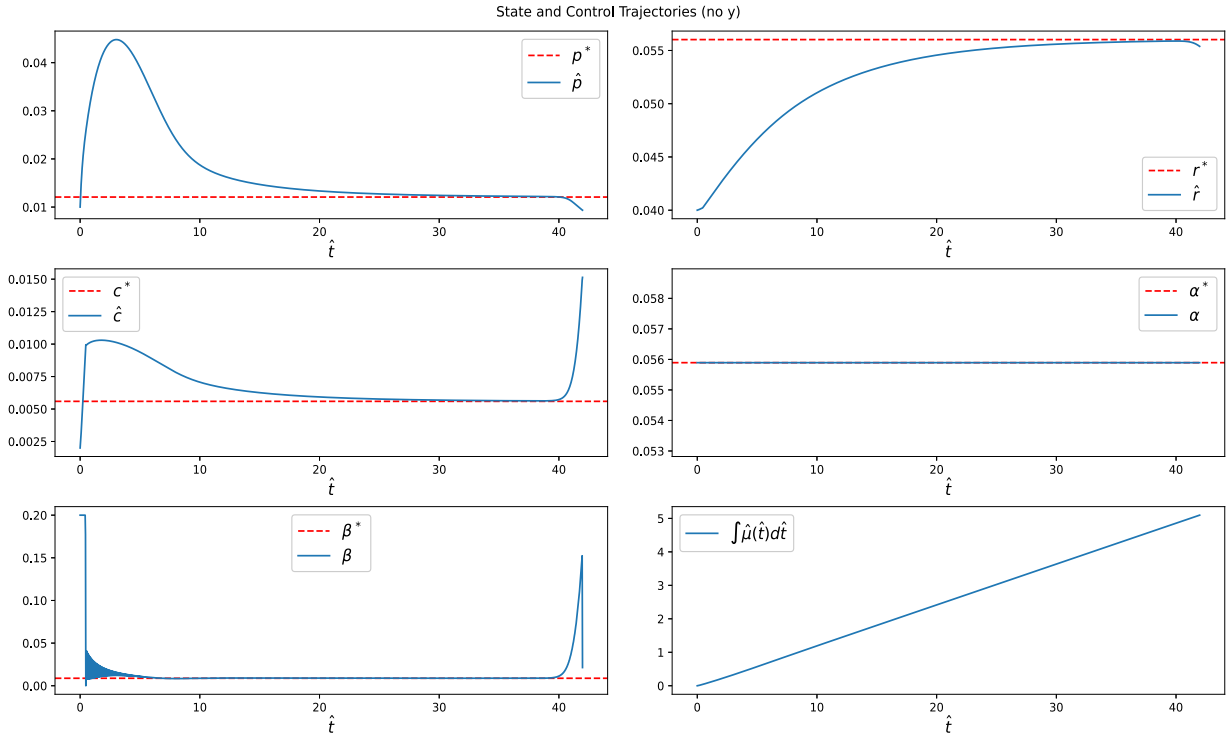

Figure 12: State variables and control input β for simulations with α fixed at its steady-state optimal value. The dotted lines represent the steady-state values, while the solid lines show the optimal trajectories. Control β exhibits bang–bang–singular behavior, entering the singular region via chattering and remaining near steady-state before deviations near the time horizon.

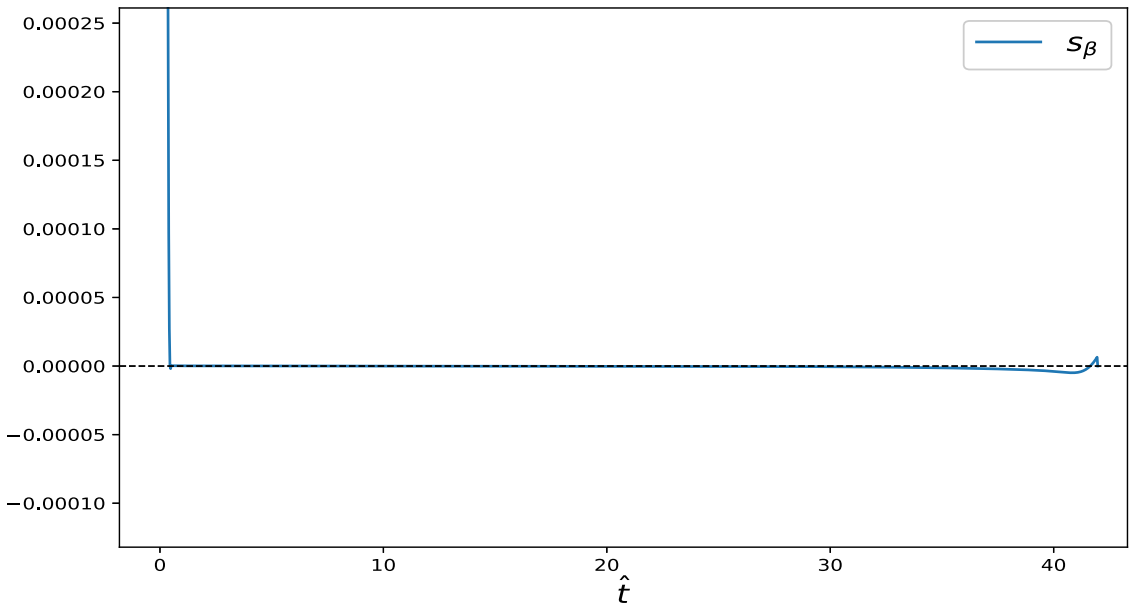

Figure 13: Switching function S_β for the scenario with α fixed at its optimal steady-state value. Zero values indicate the singular phase, showing intervals where β enters the singular regime.

When a terminal condition (11) is imposed, the system is required to reach the steady-state optimal allocation at the final time. Under this condition, both the state variables and controls remain at their steady-state values throughout the singular phase, effectively eliminating the final chattering arcs observed without the terminal condition (Fig. 14). Similar to the free-final-state case, we also examined scenarios with (i) α as the only control and (ii) β as the only control, with the remaining control fixed at its optimal steady-state value (Figs. 15 and 16). The system maintains the steady-state allocation until the final time, ensuring a smooth, sustained optimal trajectory and providing a practical justification for including the terminal constraint in the numerical simulations. The objective functional, representing total accumulated growth, is initially a little slow and then increases steadily over the simulation horizon, reflecting effective resource allocation throughout.

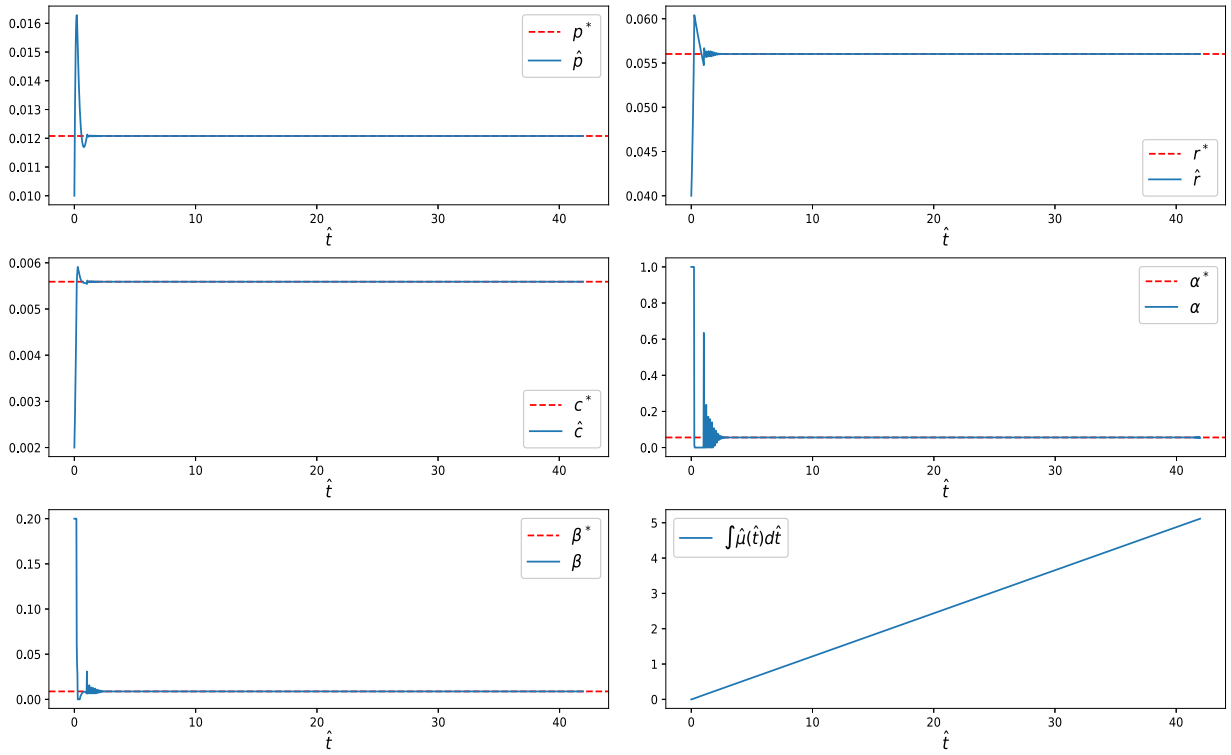

Figure 14: State variables and control inputs α and β under a terminal condition (11). The dotted lines represent the steady-state optimal values, while the solid lines show the optimal trajectories. Both controls remain at their optimal steady state allocations throughout the singular phase, keeping the system at steady state until the final time.

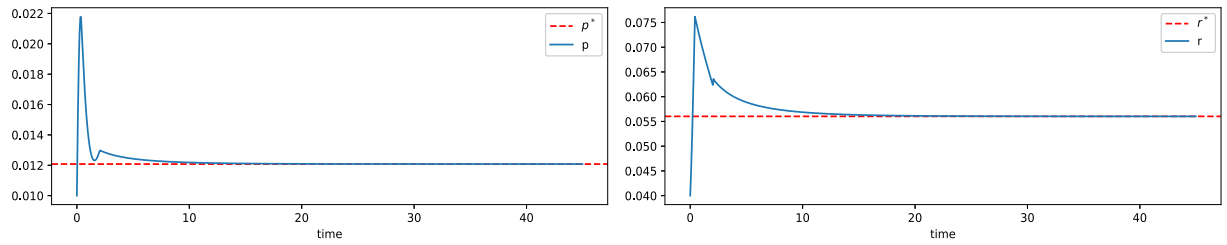

Figure 15: (Continued)

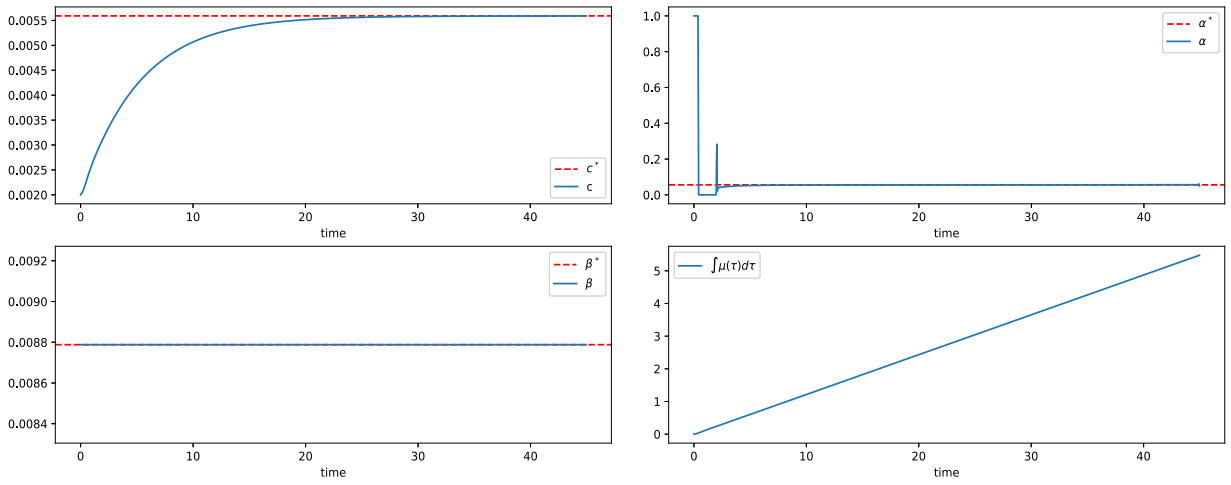

Figure 15: State variable and control input α under terminal condition (11), with β fixed at its steady-state optimal value. Dotted lines show optimal steady-state values, and solid lines show optimal trajectories. The control enters the singular phase, remaining near steady state until the final time.

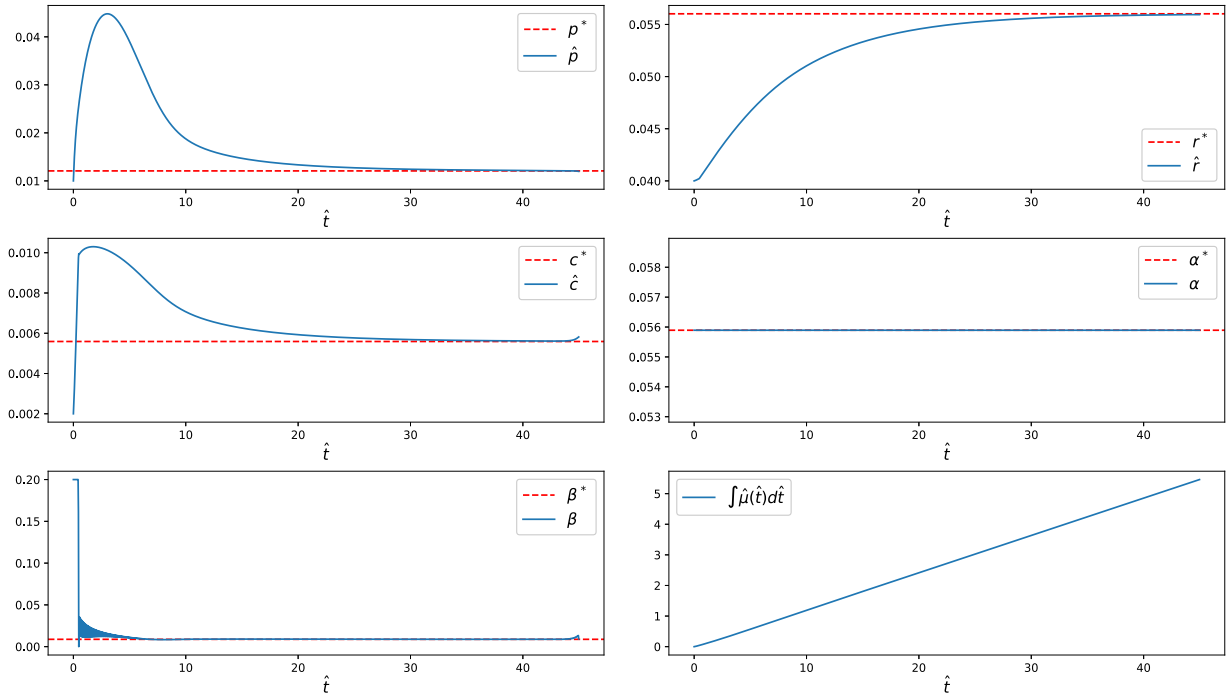

Figure 16: State variable and control input β under the terminal condition (11), with α fixed at its steady state optimal value. Dotted lines show optimal steady-state values, and solid lines show optimal trajectories. The control enters the singular phase and remains at its steady state allocation, maintaining the system near steady state until the final time.

Overall, the numerical results obtained using `CasADi` and `IPOPT` are fully consistent with the predictions of Pontryagin's Maximum Principle. From a biological perspective, this behavior reflects rapid reallocation of translational resources during initial adjustment, followed by maintenance of a balanced growth state. The singular phase corresponds to sustained optimal proteome allocation, linking the bang-bang-singular control structure to bacterial adaptation under cold conditions.

5 Conclusion

In this study, we developed and analyzed a quantitative framework to investigate how *Escherichia coli* allocates limited cellular resources under cold-shock conditions, with particular emphasis on the role of the major cold-shock protein CspA. At low temperatures, the stabilization of mRNA secondary structures inhibits translation, reducing growth. CspA acts as an RNA chaperone that alleviates these inhibitory structures, thereby partially restoring translational efficiency. However, synthesizing CspA consumes translational capacity, creating a fundamental trade-off between stress response investment and biomass production. Incorporating CspA explicitly as a competing resource demand allowed us to capture the fundamental trade-off between stress-response investment and biomass production in a coarse-grained self-replicator model.

Across the temperature range considered (13°C–19°C), steady-state analysis revealed a distinct, locally stable equilibrium allocation of precursors, ribosomes, and CspA for each temperature. The predicted optimal investment in CspA remains small but nonzero, consistent with its role as a facilitator of translation rather than a major proteomic burden. Numerical simulations confirmed that system trajectories converge robustly to the temperature-specific steady states from initial conditions, indicating that the qualitative stability structure is preserved across physiologically relevant temperatures.

At the reference temperature (15°C), we examined the structure of optimal allocation using Pontryagin's Maximum Principle. Our analysis revealed that the optimal allocation of resources exhibits a bang-bang-singular structure, where investment sharply shifts between biomass production and translational maintenance. This reflects the biological reality that bacteria must dynamically reallocate resources to respond efficiently to environmental changes, such as sudden temperature downshifts. While the exact bang-bang-singular pattern may not be fully realized in nature, it serves as a gold standard, providing a benchmark for understanding cellular decision-making and guiding the evaluation of real bacterial strategies.

Overall, this framework offers quantitative insight into how bacteria balance translational maintenance and biomass production during cold stress. By linking molecular aspects of the cold-shock response with optimal control theory, the study provides a foundation for interpreting bacterial adaptation strategies and suggests potential applications in synthetic biology and biotechnology, where improved performance at low temperatures is often desirable. Future work may include experimental validation, extension to multi-stress scenarios, the incorporation of additional biological constraints, and the development of adaptive or feedback-based strategies for quasi-optimal resource allocation. However, there are some limitations to this study: the model was developed for a restricted temperature range of 13°C–19 °C representing mild cold-acclimation conditions where $E.\ coli$ remains metabolically active and temperature effects can be approximated using Q_{10} scaling. Model predictions outside this range should be interpreted with caution, as additional constraints at lower temperatures and normal growth physiology at higher temperatures are not captured by the present formulation.

Acknowledgement: We would like to thank NASA Oklahoma Established Program to Stimulate Competitive Research (EPSCoR) Infrastructure Development, "Machine Learning Ocean World Biosignature Detection from Mass Spec" (PI: Brett McKinney), and Tandy School of Computer Science, University of Tulsa.

Funding Statement: This work was partly supported by NASA Oklahoma Established Program to Stimulate Competitive Research (EPSCoR) Infrastructure Development, "Machine Learning Ocean World Biosignature Detection from Mass Spec," (PI: Brett McKinney), Grant No. 80NSSC24M0109, and Tandy School of Computer Science, The University of Tulsa.

Author Contributions: The authors confirm contribution to the paper as follows: Saira Batool: Conceptualization, Data curation, Formal analysis, Software, Validation, Writing—original draft. Muhammad Imran: Data curation, Formal analysis, Investigation, Project administration, Resources, Writing—review & editing. Brett McKinney: Supervision, Software, Validation, Visualization, Writing—review & editing. All authors reviewed and approved the final version of the manuscript.

Availability of Data and Materials: All data supporting the findings of this study are available in the article.

Ethics Approval: Not applicable.

Conflicts of Interest: The authors declare no conflicts of interest.

References

1. Barria C, Malecki M, Arraiano CM. Bacterial adaptation to cold. Microbiology. 2013;159(Pt_12):2437–43. doi:10.1099/mic.0.052209-0.
2. Zhang Q, Li R, Li J, Shi H. Optimal allocation of bacterial protein resources under nonlethal protein maturation stress. Biophys J. 2018;115(5):896–910. doi:10.1016/j.bpj.2018.07.021.
3. Ehrenberg M, Bremer H, Dennis PP. Medium-dependent control of the bacterial growth rate. Biochimie. 2013;95(4):643–58. doi:10.1016/j.biochi.2012.11.012.
4. Serbanescu D, Ojkic N, Banerjee S. Cellular resource allocation strategies for cell size and shape control in bacteria. FEBS J. 2022;289(24):7891–906. doi:10.1111/febs.16234.
5. Trickovic B, Lynch M. Resource allocation to cell envelopes and the scaling of bacterial growth rate. Phys Biol. 2025;22(4):046002. doi:10.1101/2022.01.07.475415.
6. Dourado H, Lercher MJ. An analytical theory of balanced cellular growth. Nat Commun. 2020;11(1):1226. doi:10.1101/607374.
7. Scott M, Gunderson CW, Mateescu EM, Zhang Z, Hwa T. Interdependence of cell growth and gene expression: origins and consequences. Science. 2010;330(6007):1099–102. doi:10.1126/science.1192588.
8. Jiang W, Hou Y, Inouye M. CspA, the major cold-shock protein of *Escherichia coli*, is an RNA chaperone. J Biol Chem. 1997;272(1):196–202. doi:10.1074/jbc.272.1.196.
9. Giuliodori AM, Belardinelli R, Duval M, Garofalo R, Schenckbecher E, Hauryliuk V, et al. *Escherichia coli* CspA stimulates translation in the cold of its own mRNA by promoting ribosome progression. Front Microbiol. 2023;14:1118329. doi:10.3389/fmicb.2023.1118329.
10. Ivancic T, Jamnik P, Stopar D. Cold shock CspA and CspB protein production during periodic temperature cycling in *Escherichia coli*. BMC Res Notes. 2013;6(1):248. doi:10.1186/1756-0500-6-248.
11. Li H, Giuliodori AM, Wang X, Tian S, Su Z, Gualerzi CO, et al. Cold shock proteins mediate transcription of ribosomal RNA in *Escherichia coli* under cold-stress conditions. Biomolecules. 2025;15(10):1387. doi:10.3390/biom15101387.
12. Giuliodori AM, Di Pietro F, Marzi S, Masquida B, Wagner R, Romby P, et al. The cspA mRNA is a thermosensor that modulates translation of the cold-shock protein CspA. Mol Cell. 2010;37(1):21–33. doi:10.1016/j.molcel.2009.11.033.
13. Yegorov I, Mairet F, Gouzé JL. Optimal feedback strategies for bacterial growth with degradation, recycling, and effect of temperature. Optim Control Appl Methods. 2018;39(2):1084–109. doi:10.1002/oca.2398.
14. Imizcoz JI, Djema W, Mairet F, Gouzé JL. Optimal control of a microbial growth model by means of substrate concentration and resource allocation. IFAC-PapersOnLine. 2025;59(6):528–33. doi:10.1016/j.ifacol.2025.07.200.
15. Weiße AY, Oyarzún DA, Danos V, Swain PS. Mechanistic links between cellular trade-offs, gene expression, and growth. Proc Natl Acad Sci U S A. 2015;112(9):E1038–47. doi:10.1073/pnas.1416533112.
16. Molenaar D, Van Berlo R, De Ridder D, Teusink B. Shifts in growth strategies reflect tradeoffs in cellular economics. Mol Syst Biol. 2009;5(1):323. doi:10.1038/msb.2009.82.
17. Yabo AG. Optimal control strategies in a generic class of bacterial growth models with multiple substrates. Automatica. 2025;171(5):111881. doi:10.1016/j.automatica.2024.111881.

18. Mairet F, Gouzé JL, De Jong H. Optimal proteome allocation and the temperature dependence of microbial growth laws. npj Syst Biol Appl. 2021;7(1):14. doi:10.1038/s41540-021-00172-y.
19. Martinez G, Pachepsky YA, Shelton DR, Whelan G, Zepp R, Molina M, et al. Using the Q10 model to simulate *E. coli* survival in cowpats on grazing lands. Environ Int. 2013;54:1–10. doi:10.1016/j.envint.2012.12.013.
20. Storn R, Price K. Differential evolution—a simple and efficient heuristic for global optimization over continuous spaces. J Glob Optim. 1997;11(4):341–59. doi:10.1023/a:1008202821328.
21. Fiedler A, Raeth S, Theis FJ, Hausser A, Hasenauer J. Tailored parameter optimization methods for ordinary differential equation models with steady-state constraints. BMC Syst Biol. 2016;10(1):80. doi:10.1186/s12918-016-0319-7.
22. Strogatz SH. Nonlinear dynamics and chaos: with applications to physics, biology, chemistry, and engineering. Boca Raton, FL, USA: Chapman and Hall/CRC; 2024.
23. Yabo AG, Caillau JB, Gouzé JL. Optimal bacterial resource allocation: metabolite production in continuous bioreactors. Math Biosci Eng. 2020;17(6):7074–100.
24. Augier N, Yabo AG. Time-optimal control of piecewise affine bistable gene-regulatory networks. Int J Robust Nonlinear Control. 2023;33(9):4967–88. doi:10.1002/rnc.6012.
25. Yabo AG, Caillau JB, Gouzé JL. Optimal bacterial resource allocation strategies in batch processing. SIAM J Appl Math. 2024;84(3):S567–91. doi:10.1137/22m1506328.
26. Trélat E, Zuazua E. The turnpike property in finite-dimensional nonlinear optimal control. J Differ Equ. 2015;258(1):81–114. doi:10.1016/j.jde.2014.09.005.
27. Lenhart S, Workman JT. Optimal control applied to biological models. Boca Raton, FL, USA: Chapman and Hall/CRC; 2007.
28. Pontryagin LS. Mathematical theory of optimal processes. London, UK: Routledge; 2018.
29. Van der Schaft AJ. Symmetries in optimal control. SIAM J Control Optim. 1987;25(2):245–59. doi:10.1137/0325015.